Behavior-relevant top-down cross-modal predictions in mouse neocortex

Han, Shuting ; Helmchen, Fritjof

DOI: https://doi.org/10.1038/s41593-023-01534-x

Behavior-relevant top-down cross-modal predictions in mouse neocortex

Shuting Han[1*], Fritjof Helmchen[1,2,3*].

[1]Brain Research Institute, University of Zurich, Zurich, Switzerland. [2]Neuroscience Center Zurich (ZNZ), University of Zurich, Zurich, Switzerland. [3]University Research Priority Program (URPP), Adaptive Brain Circuits in Development and Learning, University of Zurich, Zurich, Switzerland;

[*]Corresponding authors: han@hifo.uzh.ch, helmchen@hifo.uzh.ch

Abstract

Animals adapt to a constantly changing world by predicting their environment and the consequences of their actions. The predictive coding hypothesis proposes that the brain generates predictions and continuously compares them with sensory inputs to guide behavior. However, how the brain reconciles conflicting top-down predictions and bottom-up sensory information remains unclear. To address this question, we simultaneously imaged neuronal populations in the mouse somatosensory barrel cortex and posterior parietal cortex during an auditory-cued texture discrimination task. In mice that had learnt the task with fixed tone-texture matching, presentation of mismatched pairing induced conflicts between tone-based texture predictions and actual texture inputs. When decisions were based on the predicted rather than the actual texture, top-down information flow was dominant and texture representations in both areas were modified, whereas dominant bottom-up information flow led to correct representations and behavioral choice. Our findings provide evidence for hierarchical predictive coding in the mouse neocortex.

Introduction

Predictive processing has long been an attractive theory of the mind. This theory states that the brain is organized hierarchically, with predictions generated in high-level areas passed down to lower areas, and mismatched sensory inputs that do not fit the predictions creating bottom-up flow that represents prediction errors[1]. Despite the computational attractiveness of this model, its implementation in the brain remains elusive. While reward prediction has been studied extensively[2–5], sensory prediction in the neocortex is less understood. It often originates from prior experience, typically through learnt associations with other sensory cues, and occurs across many sensory modalities[6–10]. Such prediction can increase the encoding speed and reduce the neural response to expected stimuli in primary sensory areas[6,8], facilitating decisions and behavioral output. Strong sensory predictions can also modify perception, in extreme cases causing hallucination[11–13].

One challenge in studying sensory prediction is to simultaneously observe bottom-up and top-down information. Studies targeting long-range projection axons as a proxy for top-down inputs to local populations

have demonstrated that such pathways can indeed modulate sensory perception and decision making[6,9,14]. However, studies focusing on how neuronal populations along the brain hierarchy represent and transform information, as well as how they communicate with each other, began only recently[15–20]. These studies discovered, for example, that top-down and bottom-up information are channeled through separate activity subspaces[15,16], and that the communication channels are shaped by experience or learning, especially the top-down subspace[18,19,21]. Despite these insights, it is still unknown how top-down predictions and bottom-up sensory inputs interact during behavior and affect behavioral outputs, particularly when they are in conflict.

A key area for routing primary sensory information during active behaviors is the posterior parietal cortex (PPC). PPC is densely interconnected with primary sensory areas such as visual (V1), somatosensory (S1), and auditory (A1) cortex, as well as frontal areas such as the orbitofrontal cortex and the anterior cingulate cortex, and the associative subdivision of thalamus[22]. PPC subserves a wide range of functions including multisensory integration, decision making, working memory, and navigation[22]. In particular, PPC integrates tactile, visual and auditory information in rodents[23–25] and routes relevant sensory information to frontal areas during active behaviors[26–28]. As a key area for multisensory integration, PPC is a candidate for generating cross-modal sensory predictions from previously learnt associations. Of particular relevance here is that different subdivisions of PPC engage differentially in processing distinct stimulus modalities: the rostrolateral area (PPC-RL) is activated together with S1 barrel cortex during texture discrimination, whereas the anterior area (PPC-A) activates with auditory cortex areas in an auditory discrimination task[26]. These PPC areas are critical for generating sensory associations and transforming sensory information into decisions[26,29–31], making them potential key high-level areas for generating predictions.

Here, we aim to better understand how cortical areas along the cortical hierarchy interact when sequential stimuli from two modalities (auditory and tactile) provide task-relevant information. In this case, repeatedly matching specific pairs of auditory-tactile stimuli allows the animal to form predictions about the second stimulus. It is then especially interesting to reveal how regional neural representations and cross-areal interactions are affected when conflicts between predictions and sensory inputs are imposed. Specifically, we focused on the S1 barrel field and PPC subdivisions as representative areas along the hierarchy. We designed a behavioral task with cross-modal sensory predictions (by training mice on matched tone-texture sequence pairs), and then introduced prediction conflicts by occasionally presenting mismatched tone-texture pairs. We used the behavioral choices of mice as a proxy for their perceptual representations. We found that during mismatch, when mice made decisions according to predictions, texture representation in both S1 and PPC were modified. Moreover, these changes only occurred when top-down information flow from the relevant subdivision of PPC was dominant, whereas strong bottom-up information flow from S1 led to both correct texture encoding and corresponding behavioral outcome. These results demonstrate the impact of predictions on sensory encoding and suggest that the dynamic interaction between top-down and bottom-up information shapes sensory encoding and affects perceptual choice.

Results

An auditory-cued texture discrimination task

To study sensory prediction, we developed an auditory-cued texture discrimination task for mice. Mice were trained to discriminate two textures (rough vs. smooth), each associated with a distinct preceding tone (10 kHz vs. 18 kHz). Each tone-texture sequence entailed a reward from one of the two lick ports (Fig. 1a-b). During learning, the tone-texture pairing remained fixed, allowing mice to develop specific tone-texture association ("matched trials"). Then, in expert mice, we randomly presented 10-30% tone-texture mismatches ("mismatched trials") to introduce prediction conflicts (Fig. 1b). In these trials, reward was given according to the tone, to encourage mice to engage in active predictions. For tone-texture mismatches, mice could make two types of choices: 1) choose the lick port according to the tone ("mismatch-choose-tone" or "MM→Tone" trials), indicating that the tone-based prediction, rather than the actual texture stimulus, dominated the decision; 2) choose according to the texture ("mismatch-choose-texture" or "MM→Texture" trials), indicating that the decision was made based on the actual texture rather than the tone-based prediction (Fig. 1c).

We trained 16 mice expressing GCaMP6f in L2/3 neurons (see Methods), all of which could successfully learn the task (Fig. 1d; Extended Data Fig. 1a). Compared to naïve condition, expert mice showed suppressed licking during tone presentation, and delayed decision time during texture presentation (Extended Data Fig. 1b-e), indicating that mice associated the tone-texture sequence rather than tone alone with reward. At the end of the experiment, we presented the mice with only tone or only texture, while maintaining the same task structure. With single-modality stimuli, mice still performed above chance level, albeit with lower success rate, indicating that mice integrated both sensory modalities to make decisions. Furthermore, mice performed better for only-texture compared to only-tone presentation (Fig. 1e). The latter condition resulted in a higher task disengagement rate (miss rate, Fig. 1f), suggesting that mice regard the missing texture as incomplete task structure. Finally, testing under texture-only condition with whiskers removed diminished task performance to chance level (Fig. 1e). Together, these results indicate that mice integrate tone and texture to perform the task, with texture being the most relevant stimulus, presumably due to its closer temporal link to trial outcome.

In mismatched trials, when an unexpected texture followed the tone, mice decided less likely according to the texture identity than in matched trials (Fig. 1g, Correct vs. MM→Texture; in both these trial types decisions were according to texture identity). Similarly, the tone biased the choice of mice to a degree not explainable by mere mistakes (Fig. 1g, Incorrect vs. MM→Tone; in both these trial types decisions were opposite to texture identity). When mice chose according to texture under mismatched condition, the lick probability during the texture and decision windows was slightly reduced (Fig. 1h left, Fig. 1k), indicating lower decision confidence. When mice chose according to tone, mice licked more decisively (Fig. 1h right, Fig. 1k), responded faster in general (Fig. 1i), and were more likely to lick before texture onset (Fig. 1j). It is worth noting that in most trials, for all trial types, mice started licking after texture onset (Fig. 1h), indicating that the texture was the most relevant stimulus for the task. These observations were not due to the reward rule in

mismatched condition: the observations were similar when we rewarded mismatched trials according to texture (Extended Data Fig. 1f-i). We also analyzed movements and pupil diameter of mice. While face and body movements were not significantly different across trial types, the pupil diameter was overall higher in mismatch-choose-texture trials (Extended Data Fig. 1k-m), indicating a higher arousal state that could contribute to mice paying more attention to the texture type. Overall, despite the prominence of the texture stimulus, mice do associate the auditory tone with the following texture stimulus, and the preceding auditory tone does bias the behavior and choice of mice.

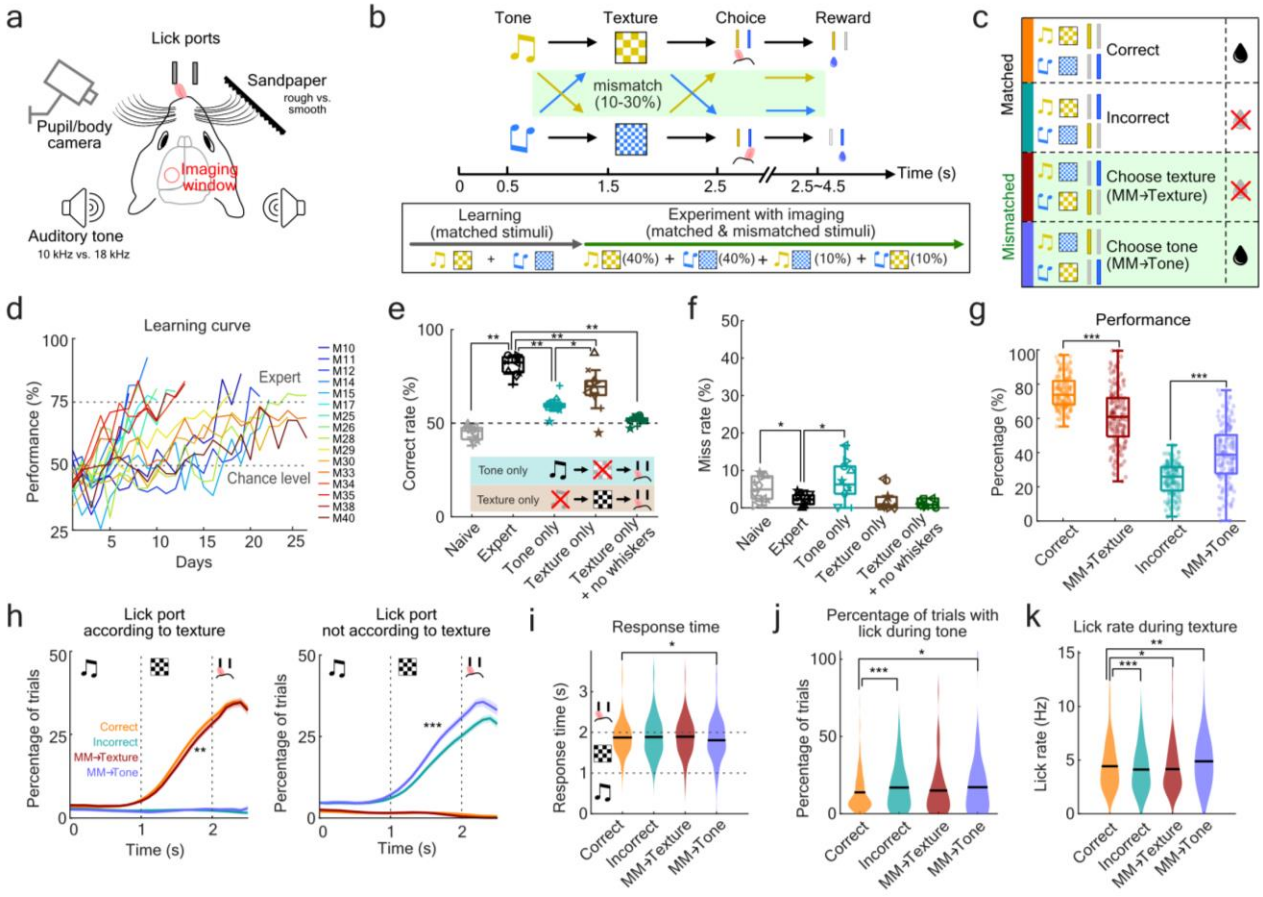

Figure 1. Mouse behavior in an auditory-cued texture discrimination task under matched and mismatched conditions. (a) Schematic of experiment setup with head-fixed mice, with a cranial window over S1 and PPC under a two-photon microscope. **(b)** Schematic of behavior paradigm. Mice were trained to discriminate two textures paired with distinct auditory tone cues. After mice became expert, tone-texture mismatch trials were introduced. The choice window lasted maximally 2-s, and reward window was triggered immediately when the mouse licked during this window. **(c)** Schematic, nomenclature and color code of different trial types. Trials were categorized based on the contingency of tone, texture, and choice. Colored bars on the left indicate the color code of each trial type. **(d)** Learning curves of all mice. M30, M33 and M40 were unstable performers (see Extended Data Fig. 1a). **(e)** Performance in single-modality experiments, in which only tone, only texture, or only texture without whiskers was presented. Markers indicate individual mice. The outlier (star) is M40 in (d). **(f)** Miss rates for experiments in (e). **(g)** Percentage of each trial type for matched and mismatched conditions. **(h)** Lick probability over trial time on the lick ports according to texture identity (left) or the opposite lick port (right), calculated as percentage of trials in each session with a lick event at each given time point. **(i)** Response time for different trial types. **(j)** Percentage of trials in each session, in which licks on the final choice spout were recorded during tone presentation. **(k)** Lick rate during texture presentation for different trial types. (e-f: n = 10 mice, 1 session per mouse, naïve was the average of first 3 sessions, expert was the average of best 3 sessions; g-k: n = 16 mice, total 148 sessions; Wilcoxon Signed-Rank test; here and in subsequent panels: *p < 0.05, **p < 0.01, ***p < 0.001; for exact p-values, see Supplementary Table 1)

Simultaneous imaging of S1 and PPC areas during the task

Using a custom-built two-area two-photon microscope[32], we simultaneously imaged population activity in S1 and PPC when expert mice performed the task (Fig. 2a). Previously, auditory and tactile stimuli were shown to recruit distinct PPC subdivisions: PPC-A (anterior) and PPC-RL (rostrolateral), respectively[26]. To study interactions of cortical areas along the sensory hierarchy, we simultaneous recorded from S1 and PPC-A (9 mice, 40 sessions) or S1 and PPC-RL (14 mice, 91 sessions; 9 mice also had S1 and PPC-A sessions) (Fig. 2b). The location of S1 and PPC areas were determined by sensory mapping as well as retinotopic mapping[33] (Extended Data Fig. 2a). We recorded in layer 2/3 across multiple (3-4) depths (100-300 µm), covering ~50-600 neurons from each population (Extended Data Fig. 2b-c; Methods). Calcium indicator fluorescence signals from individual neurons and deconvolved spike rate were extracted using Suite2p[34]. All following analysis was performed on deconvolved spike rates.

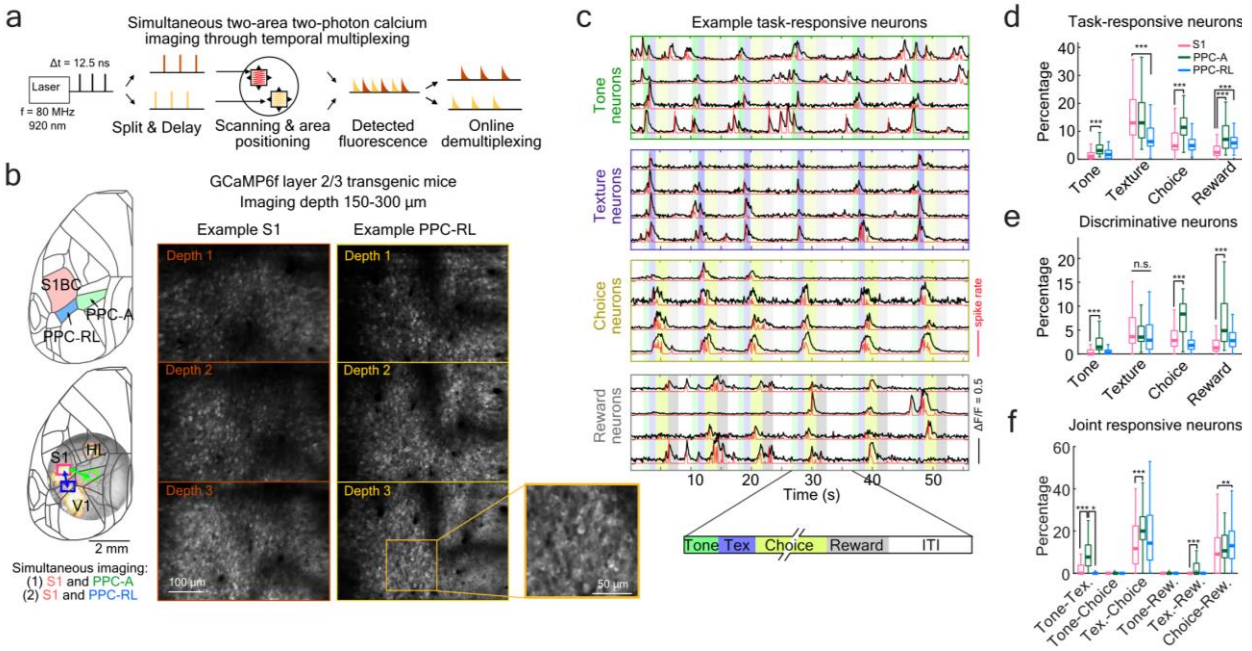

Figure 2. Simultaneous two-photon imaging of task-related S1 and PPC activity. (a) Temporal multiplexing-based simultaneous two-area two-photon imaging. Laser pulses were split into two copies, one of which was delayed by half of the pulse interval. Each copy was directed to an independently positioned field of view (FOV), and the emitted fluorescence was demultiplexed online with fast acquisition hardware. **(b)** Left: locations of S1, PPC-RL and PPC-A on the left hemisphere (top). Example widefield sensory mapping response, as well as example FOV locations, are shown in the bottom panel. Right: example FOVs of simultaneously imaged S1 and PPC-RL. **(c)** Example ΔF/F traces (black) and spike rates (red) of task-responsive neurons. **(d)** Percentage of task-responsive neurons for each task window in S1, PPC-RL and PPC-A. **(e)** Percentage of discriminative neurons for each task variable in the three areas. **(f)** Percentage of joint responsive neurons (neurons that are responsive in two task windows). The percentage was calculated as Ni⋂Nj/Ni⋃Nj, where Ni and Nj are sets of responsive neurons for task phase i and j. (S1: 14 mice, 118 sessions; PPC-RL: 14 mice, 78 sessions; PPC-A: 9 mice, 40 sessions; Wilcoxon Rank Sum test; mice and session number are the same for the following figures; Supplementary Table 1).

All three areas were engaged in the task, showing a varying degree of activation across the task windows. We identified task-responsive and discriminative neurons from matched conditions (correct and incorrect trials), using neuronal activity in each task window (Fig. 2c; Extended Data Fig. 2d; Methods). Neurons were defined as task-responsive if their activity level was significantly higher in a specific task window compared to a null distribution generated by randomly sampling frames outside of this window with matching number of frames.

Among the responsive neurons, neurons with significantly higher activity in one task condition versus the other (e.g., texture 1 vs. 2) were defined as discriminative neurons. While S1 and both PPC-A and PPC-RL displayed highest task-related activity during the texture window, PPC-A had the highest fractions of both task-responsive and discriminative neurons in the remaining tone, choice, and reward windows (Fig. 2d-e), indicating its higher position in the hierarchy. In addition, both tone and texture neurons were more abundant in the medial part of PPC-A (Extended Data Fig. 2e). PPC-RL was less involved than PPC-A during sensory processing, but was also more engaged than S1 after reward delivery. In PPC-A, joint responsive neurons for tone and texture accounted only for a small percentage. Texture and choice, however, shared ~20% of overlapping neurons (Fig. 2f). Overall, S1 was most tuned to texture processing, PPC-A was engaged throughout the trial time, and PPC-RL was involved in texture and reward processing.

Tone-texture mismatch alters texture neuron tuning

We first asked whether tone-based prediction could alter texture-evoked responses of single neurons. To answer this question, we analyzed the response amplitude of tone- and texture-discriminative neurons. While tone-discriminative neurons showed differential responses to the distinct tones, they did not show significant trial type-dependent selectivity (Extended Data Fig. 3). In contrast, the activity of texture-discriminative neurons could be altered by the tone. In S1, texture-discriminative neurons showed texture selectivity only in mismatch-choose-texture trials; when mice chose according to tone, these neurons showed mixed preferences, responding to a combination of expected and actual texture (Fig. 3a-c, top panels). Similar results were obtained in PPC-RL (Fig. 3a-c, bottom panels). In PPC-A, the texture-discriminative neurons showed strong preference to the expected rather than the actual texture when mice chose according to tone, but not when they chose according to texture (Fig. 3a-c, middle panels). This could not be explained by the choice selectivity of

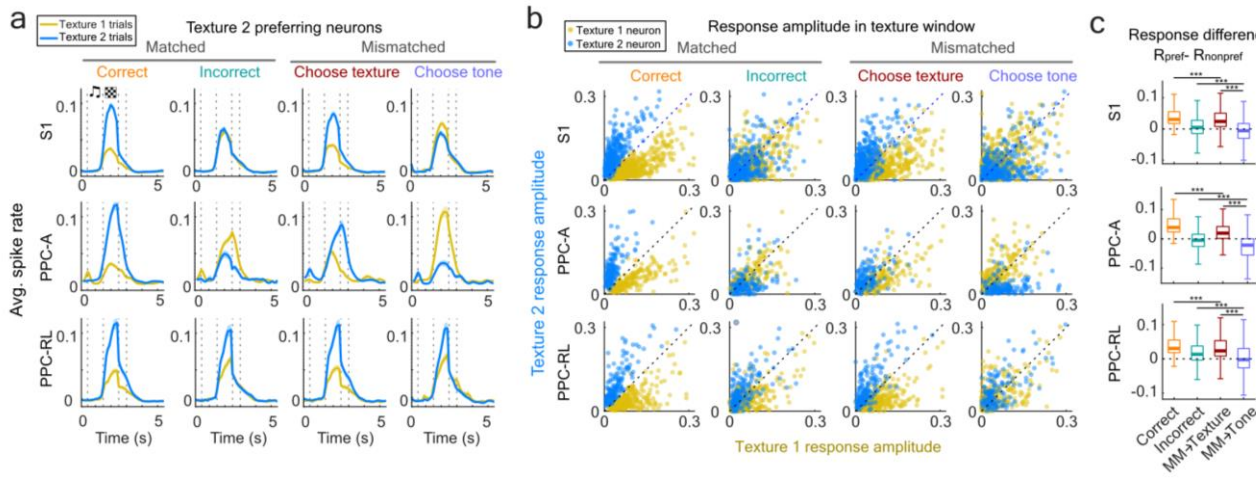

Figure 3. Tone-texture mismatch alters neuronal tuning to texture. (a) Average normalized spike rate of texture 2 discriminative neurons in S1, PPC-RL and PPC-A, in matched and mismatched trials. The spike rate of each neuron was normalized to be between 0 and 1 within each session. **(b)** The mean response amplitudes of all texture discriminative neurons in the texture window. Plots are shown across areas (rows) and trial types (columns). Each dot represents the responses of one neuron in one imaging session. **(c)** Selectivity index of the texture discriminative neurons during texture window, in different trial types. Selectivity index was calculated as the difference between the average response to the preferred texture and the average response to the non-preferred texture. (S1 1486 neurons; PPC-A 400 neurons; PPC-RL 618 neurons; Wilcoxon Rank-Sum test; Supplementary Table 1)

texture neurons or licking behavior, because we observed the same effect in PPC-A texture neurons that were not choice-selective as well as in trials with no early licks (Extended Data Fig. 4). To further exclude the influence of choice-related activity, we applied a GLM model to identify texture and choice neurons from the mean activity in the texture window, which yielded a similar number of texture and choice neurons and revealed similar texture selectivity change in mismatch-choose-tone trials (Extended Data Fig. 5). It is worth noting that in all our analysis, this inverted texture preference is distinct from the response distribution observed for incorrect trials, where the texture-choice pairing is the same (choice not according to the texture). These results provide strong evidence that tone-based prediction can shift the texture representation of individual neurons in PPC-A to the expected texture, while disrupting the texture representation in PPC-RL and S1.

Tone-texture mismatch alters population encoding

To further investigate encoding of different task variables in neuronal populations of these three areas and representational changes, we trained linear support vector machine (SVM) decoders on the population activity patterns to discriminate tone, texture, choice, and reward (Fig.4a-e; Extended Data Fig. 6a-c). Each decoder was trained and cross-validated using the time-concatenated spike rates of all neurons from the corresponding task window (e.g., texture window for the texture decoder; Fig. 4a) and from matched trials (correct and incorrect trials). Each classifier defines a hyperplane that best separates the two variables; by projecting the population firing rate onto the orthogonal axis of this hyperplane, or the "projection axis", we could estimate the encoding strength of the task variables over trial time[10] (Fig. 4a; Methods).

Among the three areas, PPC-A encoded tone information best (Fig. 4b, top; Fig. 4c), consistent with PPC-A showing the highest fraction of tone-tuned neurons. While tone encoding was stronger in the tone window, it persisted after texture onset (Fig. 4d). Interestingly, tone encoding strength coincided with behavioral choice: in mismatch-choose-texture trials, PPC-A tone encoding was weaker compared to correct trials (Fig. 4c), but not in mismatch-choose-tone trials. In the latter case, the tone (and thus the expected texture) was still decodable during texture presentation (Fig. 4d, middle). We observed similar results in S1 and PPC-RL despite their weaker tone encoding. These observations are consistent with our findings that the tone could bias the behavior and choice of mice.

All three areas strongly encoded texture (Fig. 4b, bottom). Consistent with the results in single neurons, in mismatched trials, the actual texture was encoded by the populations only when mice chose texture, although weaker compared to correct trials; when mice chose tone, the expected texture was encoded instead (Fig. 4e). The timing of texture encoding is also worth noting. In matched correct trials, the actual texture was encoded slightly before texture onset, indicating an active ongoing prediction (Fig. 4b, bottom left). However, in mismatch-choose-texture trials, although the texture was encoded correctly, this early texture encoding was absent (Fig. 4b, bottom middle right). In addition, PPC-A texture encoding lagged behind S1 and PPC-RL, suggesting that the integration of texture and tone stimuli was impaired by the mismatched tone, an effect

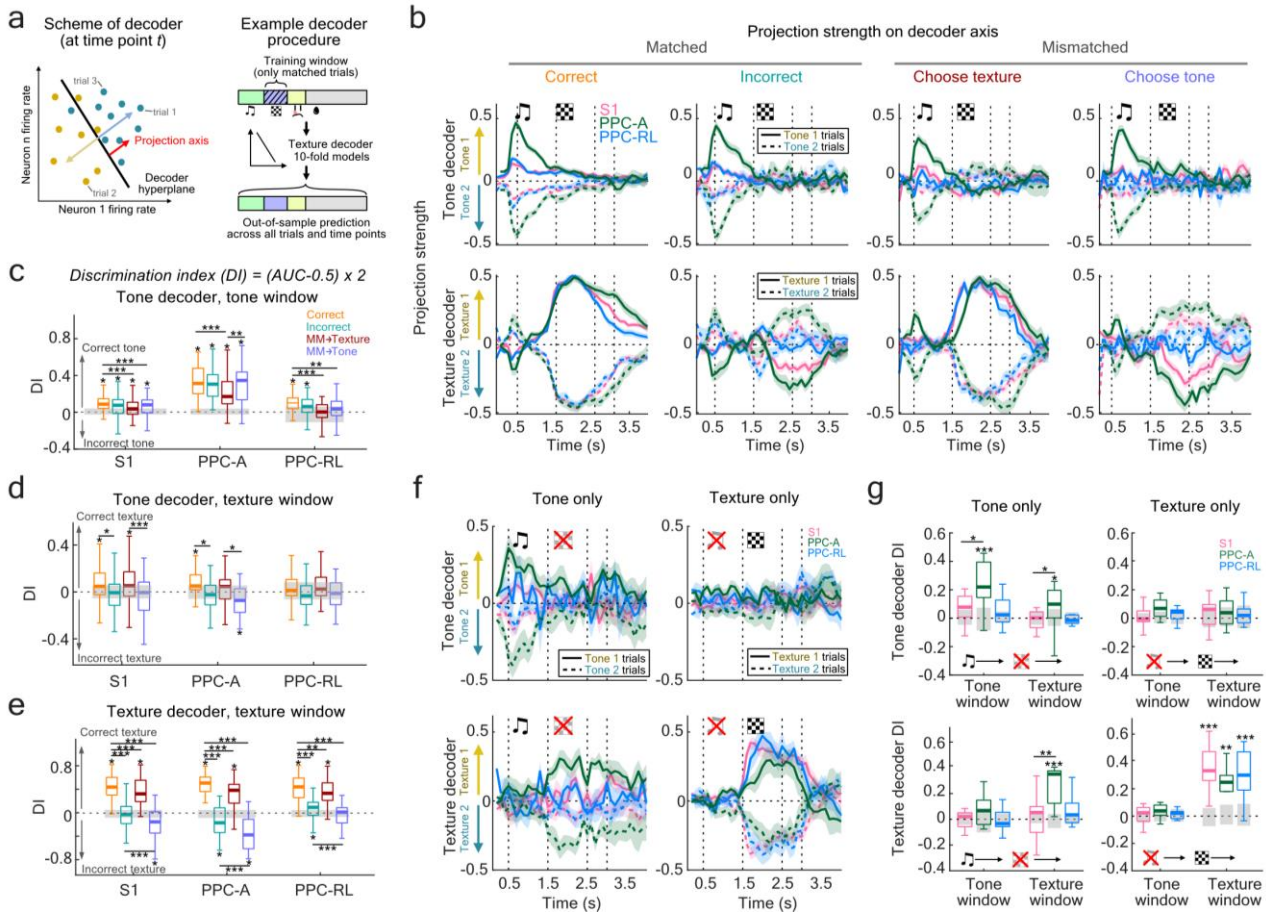

Figure 4. Tone-texture mismatch alters texture encoding in S1 and PPC populations. **(a)** Left: scheme of the decoders. Black line represents the decoder hyperplane; yellow and teal dots represent the neuronal population activity at a given time point in the trial; each dot was projected onto the orthogonal axis of the decoder hyperplane to represent the decoder confidence. Right: example procedure for texture decoding. **(b)** Neuronal population decoding of tone (top) and texture (bottom). Sensory encoding is represented by projection strength on the axes of linear decoders trained to discriminate tone and texture, in the tone and texture window, respectively. Line colors indicate area identity (magenta: S1; green: PPC-A; blue: PPC-RL); solid and dash lines indicate stimulus identity in the trial. **(c)** Discrimination index (DI) of tone decoder in the tone window. Stars above each box indicate significance compared to shuffled data (gray bars), for which neurons identities were shuffled, while trial and time correspondences were kept the same. Stars across boxes indicate comparison between trial types. **(d)** DI of tone decoder in texture window. **(e)** DI of texture decoder in texture window. **(f)** Decoder projection strength of tone (top row) and texture (bottom row) in single-modality experiments. **(g)** DI of tone decoder and texture decoder in single-modality experiments, in tone window and texture window, separately. Stars represented as in (c). (S1: 14 mice, 118 sessions; PPC-RL: 14 mice, 78 sessions; PPC-A: 9 mice, 40 sessions; Wilcoxon Rank Sum test was used for comparison with shuffled data, Wilcoxon Signed-Rank test for comparison between trial types; Supplementary Table 1)

particularly strong in PPC-A. On the other hand, in mismatch-choose-tone trials, the expected texture was encoded slightly before texture onset, and texture encoding in PPC-A preceded that of S1 and PPC-RL (Fig. 4b, bottom right; see also Extended Data Fig. 6c). These results indicate that the tone facilitated the encoding of the expected texture. This early texture encoding was not due to choice-related activity, as choice could not be decoded during the tone window in these trials (Extended Data Fig. 6b). In addition, texture decoder axes of incorrect trials did not resemble that of mismatch-choose-tone trials (Extended Data Fig. 6f). These results suggest that tone information in PPC-A led to encoding of the expected texture across S1 and PPC.

We next wondered whether the tone alone was sufficient to evoke predictive texture encoding. We trained linear classifiers for tone-only and texture-only sessions, and indeed found that tone alone led to correct

texture encoding in PPC-A (Fig. 4f-g, left). In contrast, the lack of a preceding tone reduced texture encoding speed and strength in PPC-A (Fig. 4f-g, right), but choice engaged both S1 and PPC (Extended Data Fig. 6d-e). Thus, PPC-A is able to generate predictive texture information from the preceding tone, likely through multisensory integration mechanisms, and it serves as a center for routing and transforming sensory information into decisions.

Inter-areal interaction between S1 and PPC during task

We next asked if such predictive information could be explained by top-down and bottom-up interactions between S1 and PPC areas. We started by characterizing the interaction structure of S1 and PPC populations during the task. To measure the population interactions, we used canonical correlation analysis (CCA) due to its symmetric way of treating the two populations. CCA has been applied to analyze the inter-areal interactions in several recent studies[16,17,19]. Conceptually, the activity of a neuronal population can be represented in a high-dimensional space, where each dimension represents the activity of one neuron in this population. For simultaneous activity of two populations, CCA finds pairs of dimensions that maximize the

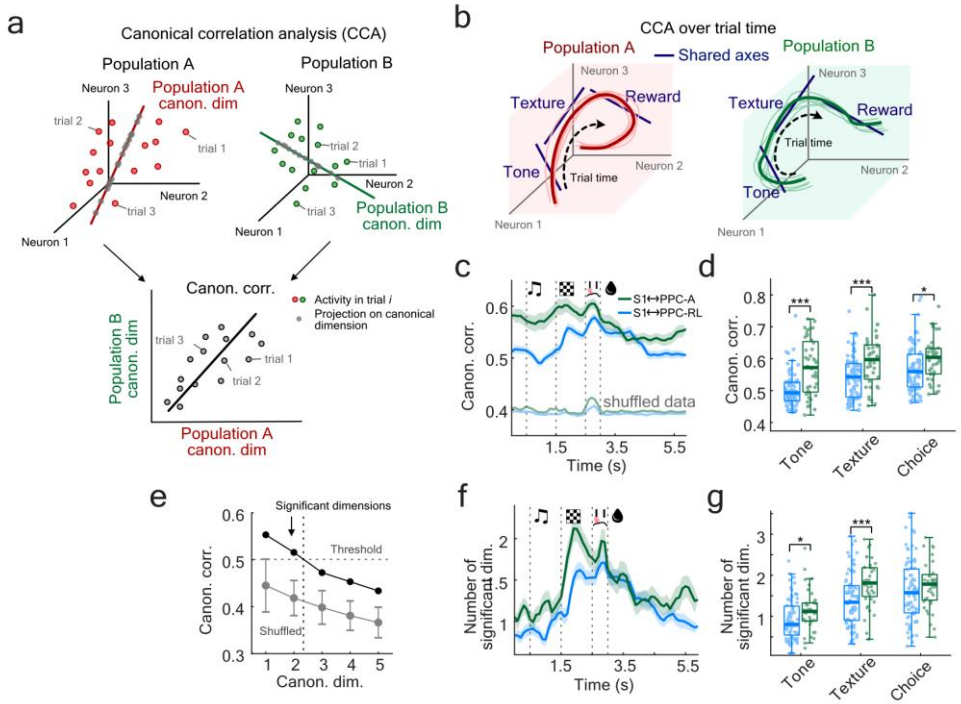

Figure 5. Interaction pattern of S1 and PPC areas during the behavioral task. (a) Illustration of canonical correlation analysis (CCA). The activity of each neuronal population can be represented as points in a high-dimensional space, where each dimension represents the activity of one neuron in this population. At a given time point in the trial, CCA identifies a set of canonical dimensions through linear combinations of variables from the two populations that have maximum correlation. **(b)** Illustration of defining separate CCA axes over the trial time. **(c)** Top canonical correlation between S1 and PPC-A (green), and S1 and PPC-RL (blue). Light colors indicate shuffled correlation, where only the trial correspondence between the two areas were shuffled, while trial structure was kept the same. **(d)** Average canonical correlation strength of (c) in each task window. **(e)** Number of significant interaction dimensions were determined by generating shuffled correlations and defining a threshold (mean + 3 S.D.) using the first correlation values. Canonical dimensions in real data with correlations higher than this threshold were considered significant. Example is from one imaging session. **(f)** Number of significant dimensions in S1 and PPC-A, and S1 and PPC-RL pairs. **(g)** Average number of significant dimensions of (f) in each task window. (S1↔PPC-A: 9 mice, 40 sessions; S1↔PPC-RL: 13 mice, 71 sessions; Wilcoxon Rank Sum test; Supplementary Table 1)

correlation between the projections of the two populations (Fig. 5a; Methods). These pairs of dimensions (canonical dimensions) define the shared interaction axes of the two populations at this time point.

Stable CCA models depend on having sufficient amount of data (time points) compared to the number of variables (neurons)[35]. To increase computation stability, we first applied principal component analysis (PCA) to both populations and kept the first 30 components. Since we are interested in the population interaction structure, we also subtracted the stimulus-triggered average, keeping only the residual activity that captures trial-to-trial co-variation. To capture the dynamic interaction over trial time, we applied CCA to a 0.5-s sliding window (Fig. 5b). Overall, the interaction between S1 and PPC-A was stronger than S1 and PPC-RL (Fig. 5c-d). We further characterized the communication subspace between S1 and PPC by computing the number of significant canonical dimensions, where the canonical correlation is above chance level. Consistent with previous reports[15,16], S1 and PPC overall interacted in a low-dimensional space, with S1 and PPC-A interacting in more dimensions than S1 and PPC-RL during tone and texture windows (Fig. 5e-g), indicating PPC-A was more involved in sensory processing during the task.

Top-down and bottom-up interactions govern behavioral choice

In behavioral tasks, sensory information flows through the cortical hierarchy to generate decisions. For our task, we asked whether the behavioral choice of mice under mismatch condition could be explained by the net effect of top-down (prediction) and bottom-up (sensory) information flow. Conceptually, mismatch-choose-texture trials could be explained by stronger bottom-up information from S1 than top-down information from in PPC, whereas mismatch-choose-tone trials could be explained by the opposite. To test this hypothesis, we measured the strength of bottom-up and top-down information flow by introducing a temporal lag in CCA. We defined bottom-up strength by moving the S1 activity window ahead of PPC and averaging the top canonical correlation across lags (over 0.3 s), and top-down strength by moving PPC activity ahead of S1, respectively (Fig. 6a). We represented net information flow by an index that was defined as difference between bottom-up and top-down strengths normalized by the total interaction strength (Fig. 6a).

In matched trials, S1 and PPC-A interaction showed strong bottom-up dominance during texture presentation (Fig. 6b,d-e, correct). In mismatch-choose-texture trials, both tone and texture windows were dominated by bottom-up information (Fig. 6b,d-e, MM→Texture), coinciding with slightly elevated bottom-up flow during the pre-stimulus window (Fig. 6d-e; 0.029±0.014 vs 0.006±0.016) and a higher arousal state in these trials (Extended Data Fig. 1j,m). In contrast, in mismatch-choose-tone trials, tone presentation was accompanied by top-down information flow, which persisted throughout texture presentation (Fig. 6b,d-e, MM→Tone). This top-down dominance was also observed from PPC-RL to S1 during tone presentation (Fig. 6c,f-g), indicating an internal state that emphasized top-down inputs.

The information flow between S1 and PPC showed similar patterns in single-modality experiments (Extended Data Fig. 7). In tone-only sessions, the population interaction resembled that of mismatch-choose-tone trials: top-down flow from PPC-A to S1 in the tone window that persisted throughout the texture window (without

texture), consistent with a role of PPC-A in tone-based predictions. In texture-only sessions, bottom-up flow from S1 to PPC-A during texture presentation occurred instead, resembling the interaction observed for mismatch-choose-texture trials. To exclude the possibility that these observations were specific to the CCA method, we alternatively computed population interaction strength with Pearson correlation. Overall, all results were reproduced, although Pearson correlation does not capture the optimal interaction between populations (Extended Data Fig. 8).

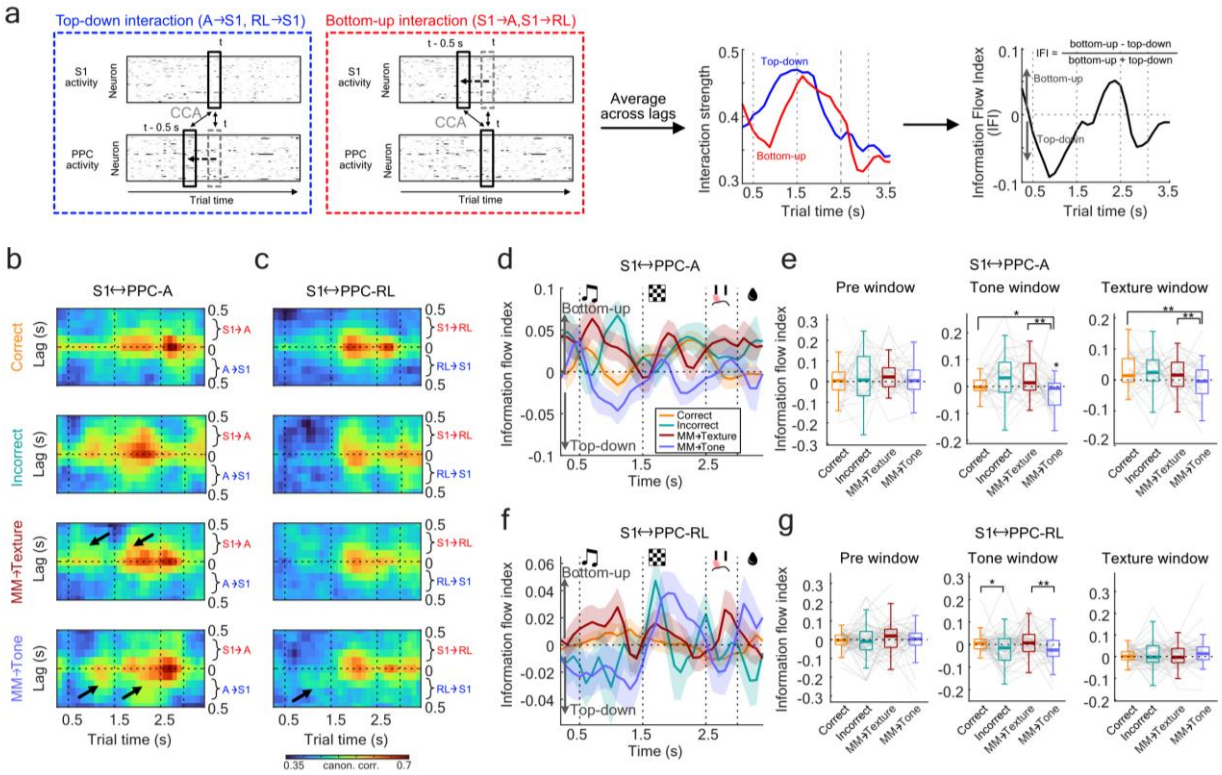

Figure 6. Top-down and bottom-up interactions between S1 and PPC areas during prediction mismatches. (a) Top-down interaction strength (PPC-A/RL to S1) was calculated by the average canonical correlation with a negative lag for PPC, and bottom-up interaction strength was calculated by the average correlation with a negative lag for S1 (left and middle panels). The direction and strength of S1-PPC interaction was characterized by the information flow index (IFI), defined as ratio of the difference between the two interactions to their sum (right panel). **(b)** Lagged canonical correlation between S1 and PPC-A, averaged across all sessions, for different trial types. **(c)** Information flow index computed from (b). **(d)** Quantification of information flow index between S1 and PPC-A. **(e)** Lagged canonical correlation between S1 and PPC-RL, averaged across all sessions, for different trial types. **(f)** Information flow index computed from (e). **(g)** Quantification of information flow index between S1 and PPC-RL. (S1↔PPC-A: 9 mice, 40 sessions; S1↔PPC-RL: 13 mice, 71 sessions; Wilcoxon Signed-Rank test; Supplementary Table 1)

To investigate whether such inter-areal interactions could be reflected by the response strength of S1 and PPC on a single-trial basis, we compared the normalized decoder projection strength of S1 and PPC-A in individual trials. While texture encoding strengths of S1 and PPC-A were similar in correct and mismatch-choose-texture trials, PPC-A showed stronger texture encoding than S1 in mismatch-choose-tone trials (Extended Data Fig. 9a-b). In the latter trials, the encoding coefficient of PPC-A tone response vs. S1 texture response was also elevated, indicating that the tone in PPC-A was weighted more than the texture information in S1 compared to other trial types (Extended Data Fig. 9c-d). Additionally, the texture/tone encoding coefficient within PPC-A was higher in mismatch-choose-texture and lower in mismatch-choose-tone trials, indicating that in PPC-A

texture was weighted more in mismatch-choose-texture trials, whereas tone was weighted more in mismatch-choose-tone trials (Extended Data Fig. 9e-f). These findings further support our observation of different top-down and bottom-up interactions underlying these conditions.

Our task design allowed the mice to rely in their behavior either more on tone-based prediction or more on the texture input. We wondered whether these different states were accompanied by different neuronal representations even in correct trials, where tone and texture were paired normally. We approximated the state of mice from their choices under mismatch condition. We defined texture-preferring sessions as the top 10 sessions where mice were more prone to choose texture in mismatch condition, and tone-preferring sessions as the top 10 sessions where mice were more prone to choose tone (Extended Data Fig. 10a). We observed both behavioral and neural differences between these two sets of sessions. Behaviorally, mice showed slightly shorter response time, higher probability of licking during tone, and higher lick rate during texture presentation in tone-preferring vs. texture-preferring session (Extended Data Fig. 10b-e). On the neuronal level, in tone-preferring sessions, with comparable numbers of tone neurons in S1 and PPC-A, tone decoding was stronger and top-down information flow from PPC-A to S1 was enhanced, suggesting a more efficient transfer of tone information. On the other hand, in texture-preferring sessions, S1 featured more texture neurons, weaker predictive texture encoding, slower texture encoding, and slightly stronger bottom-up flow (Extended Data Fig. 10f-n). These differences suggest a flexible reconfiguration of S1 and PPC populations according to behavioral state.

Together, our results demonstrate that the dynamic interactions between S1 and PPC can shape sensory representation and govern the behavioral choices of mice (Fig. 7).

Discussion

We utilized a two-area two-photon microscope to study the interaction between a primary sensory area (S1) and the next-higher association area (PPC) during an auditory-cued texture discrimination task. We focused on cortico-cortical interactions underlying cross-modal predictive processing, by introducing tone and texture mismatches to induce conflicts between tone-based top-down texture predictions and bottom-up tactile input. When predictions dominated sensory inputs, as in trials in which mice decided based on tone instead of actual texture identity, we found that PPC-A encoded the expected texture, while in S1 both single-cell and population encoding of texture were disrupted. There was also stronger top-down information flow from PPC-A to S1. When tactile input dominated predictions, as reflected by texture-based choices, texture encoding in S1 and PPC remained unchanged, and bottom-up information flow from S1 to PPC-A was stronger (Fig. 7). Overall, our results provide evidence for a cortical implementation of predictive processing in the context of multisensory-driven decision making.

Although predictive processing provides an attractive framework for understanding key brain functions, the specific neural circuits involved are yet to be fully understood. With experience, primary sensory cortices can develop specific predictions that impact stimulus responses: expected stimuli are suppressed, and unexpected

stimuli are amplified[6,7,36,37]. This occurs for both redundant unimodal stimulation[7,36,37] and multi-modal stimulation where animals associate two stimuli[6,13]. Such predictions can be conveyed directly between sensory cortices[6], but also depend on long-range projections from higher areas[7,14,38]. Whereas frontal higher areas have been extensively studied in contextual sensory processing[7,37,39], posterior association areas received less attention. Frontal areas can modulate the activity in posterior areas of single sensory modalities through long-range projections[9,40]. Posterior association areas, in contrast, may integrate multiple sensory modalities and send processed information to primary as well as frontal areas. Here, we provide evidence for such a process: PPC-A formed an association between paired sensory stimuli and carried sufficient predictive information based on an initial tone to encode the expected texture.

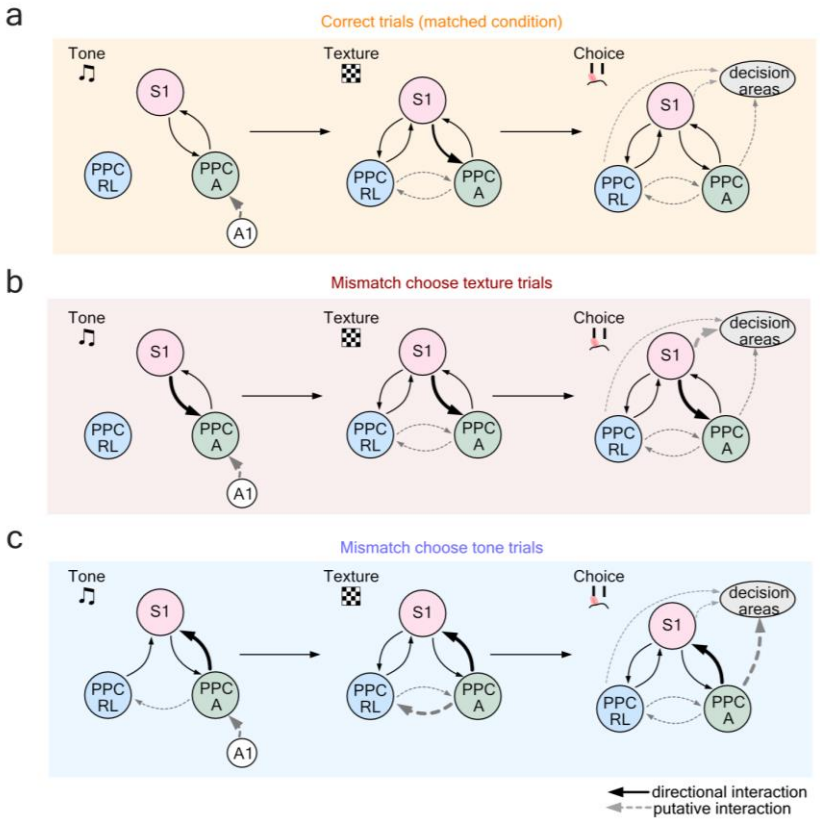

Figure 7. A model of S1, PPC-A, and PPC-RL interactions during the behavioral task. (a) In the correct trials, tone information is encoded in PPC-A, potentially through inputs from auditory cortex (A1). PPC-A generates and communicate texture prediction with S1. During the texture presentation, S1 sends texture information to PPC-A, while all three areas are involved in the processing and transformation of texture information. The decision is formed through coordinated efforts from S1 and PPC. **(b)** In mismatch-choose-texture trials, mice are in a state that attends more to S1 inputs. Texture information in S1 is sent to PPC-A, and choice is made according to actual texture. **(c)** In mismatch-choose-tone trials, tone induces strong texture prediction in PPC-A, which is sent to S1 during the tone and texture windows, overwriting the actual texture information in S1. Choice is made according to the predicted texture. Solid arrows represent directional interactions between recorded areas, dashed arrows represent putative interactions between pairs of areas that were not recorded simultaneously in this study.

How cortical areas communicate with each other, and what information is exchanged during behavior, are still open questions. Direct projections from higher cortical areas to primary sensory areas can carry specific task-related information such as expected stimulus and reward[7,9,14], providing one mechanism for how top-down predictions affect responses in primary areas. Recent studies demonstrated that interactions between primary

and higher areas usually occur in low-dimensional subspaces that do not necessarily align with the stimulus-encoding subspace[15,41], and that such interactions dynamically vary throughout stimulus presentation and behavioral tasks[16–19]. Our study adds to these findings by showing that the task-relevant variables are encoded in low-dimensional subspaces in S1 and PPC, and that the dominance of either top-down or bottom-up processing corresponds to perceptual choices during the task. These findings are consistent with the predictive processing theory and reveal mechanisms underlying cortical information transformation and communication. Specifically, we observed that the disrupted texture encoding in S1 is accompanied by stronger top-down information flow from PPC. Our multi-modal task design contributes to this observation, because PPC is involved in multisensory processing[22,23,25,42] and therefore is well-positioned to develop cross-modal predictions. On the circuit level, such predictions could be implemented by disinhibition through top-down projections: in PPC as well as in primary areas, inhibitory interneurons play a key role in suppressing expected stimuli and augmenting unexpected stimuli[23,43,44]. Other brain areas such as the thalamus might be involved as well: higher-order thalamic nuclei are interconnected with many cortical areas[20,45], providing another information routing station for processing of sensory conflicts by comparing top-down and bottom-up information.

In our task design, predictive processing is likely implemented through a multisensory integration process. We chose to use the term 'predictive processing' because it adequately describes the specific sensory association process, with two sensory modalities engaged sequentially such that a preceding tone is stably associated with a subsequent texture. Other forms of multisensory integration processes, for example resolving conflicting simultaneous auditory and visual inputs that underlie conflicting reward rules[23,46], do not necessarily involve specific sensory predictions. Furthermore, predictive processing can be implemented through other mechanisms as well. For example, reward predictions[2,5,8] and unimodal sensory predictions (e.g. mismatch negativity)[37,47] likely involve different neural circuits rather than the association cortex.

The composition and exact locations of rodent PPC and its subregions are still a topic of debate[22,26,48]. Historically, rodent PPC has been described as a part of higher visual areas, with PPC-RL largely overlapping with VISrl, and PPC-A overlapping with VISam[33,48]. However, PPC not only receives visual input, but also extensive inputs from somatosensory, auditory and olfactory cortices, as well as higher cortical areas[22,49]. Most PPC studies so far defined PPC as a single area with varying coordinates, leading to contradictory results in some cases[23,50–52]. In our study, PPC-A and PPC-RL exhibited different task relevance, and both tone and texture neurons were more enriched towards the medial PPC. This coincides with the reports that PPC contains modality-specific subregions along the medial-lateral axis[26,49], but also suggests a functional reorganization of PPC through learnt multisensory pairing[53]. PPC is not only a center for multisensory processing, but also participates in decision making [29,50,54,55]. Recent literature has shown that a topographic difference exists between the anterior and mediomedial regions of the PPC in encoding decisions[56]. Therefore, subregions in PPC likely serve as a continuum of intermediate routing stations of weighted sensory

information flow towards frontal areas, and top-down information back to sensory cortices. Further work is required to characterize in detail the specific roles of PPC subregions and their interactions.

Acknowledgements

We thank Philipp Bethge for managing transgenic mouse lines, Fabian Voigt and Hansjörg Kasper for help with optics, and Martin Wieckhorst for the behavior training software. We also thank Christopher Lewis, Jerry Chen and Jordan Hamm for their feedback on the manuscript. This work was supported by a Sinergia grant from the Swiss National Science Foundation (CRSII5_180316; to F.H.) and a UZH Forschungskredit grant (K-41220-07-01; to S.H.). F.H. received funding from the University Research Priority Program (URPP) "Adaptive Brain Circuits in Development and Learning" (AdaBD).

Author contributions

S.H. and F.H. conceived the study and designed the experiments. S.H. performed the experiments and analyzed the data. S.H. and F.H. wrote the manuscript.

Competing interests

The authors declare no competing interests.

Figure Captions and Legends

Figure 1. Mouse behavior in an auditory-cued texture discrimination task under matched and mismatched conditions. (**a**) Schematic of experiment setup with head-fixed mice, with a cranial window over S1 and PPC under a two-photon microscope. (**b**) Schematic of behavior paradigm. Mice were trained to discriminate two textures paired with distinct auditory tone cues. After mice became expert, tone-texture mismatch trials were introduced. The choice window lasted maximally 2-s, and reward window was triggered immediately when the mouse licked during this window. (**c**) Schematic, nomenclature and color code of different trial types. Trials were categorized based on the contingency of tone, texture, and choice. Colored bars on the left indicate the color code of each trial type. (**d**) Learning curves of all mice. M30, M33 and M40 were unstable performers (see Extended Data Fig. 1a). (**e**) Performance in single-modality experiments, in which only tone, only texture, or only texture without whiskers was presented. Markers indicate individual mice. The outlier (star) is M40 in (d). (**f**) Miss rates for experiments in (e). (**g**) Percentage of each trial type for matched and mismatched conditions. (**h**) Lick probability over trial time on the lick ports according to texture identity (left) or the opposite lick port (right), calculated as percentage of trials in each session with a lick event at each given time point. (**i**) Response time for different trial types. (**j**) Percentage of trials in each session, in which licks on the final choice spout were recorded during tone presentation. (**k**) Lick rate during

texture presentation for different trial types. (e-f: n = 10 mice, 1 session per mouse, naïve was the average of first 3 sessions, expert was the average of best 3 sessions; g-k: n = 16 mice, total 148 sessions; Wilcoxon Signed-Rank test; here and in subsequent panels: *$p < 0.05$, **$p < 0.01$, ***$p < 0.001$; for exact p-values, see Supplementary Table 1)

Figure 2. Simultaneous two-photon imaging of task-related S1 and PPC activity. (**a**) Temporal multiplexing-based simultaneous two-area two-photon imaging. Laser pulses were split into two copies, one of which was delayed by half of the pulse interval. Each copy was directed to an independently positioned field of view (FOV), and the emitted fluorescence was demultiplexed online with fast acquisition hardware. (**b**) Left: locations of S1, PPC-RL and PPC-A on the left hemisphere (top). Example widefield sensory mapping response, as well as example FOV locations, are shown in the bottom panel. Right: example FOVs of simultaneously imaged S1 and PPC-RL. (**c**) Example $\Delta F/F$ traces (black) and spike rates (red) of task-responsive neurons. (**d**) Percentage of task-responsive neurons for each task window in S1, PPC-RL and PPC-A. (**e**) Percentage of discriminative neurons for each task variable in the three areas. (**f**) Percentage of joint responsive neurons (neurons that are responsive in two task windows). The percentage was calculated as $N_i \cap N_j / N_i \cup N_j$, where N_i and N_j are sets of responsive neurons for task phase *i* and *j*. (S1: 14 mice, 118 sessions; PPC-RL: 14 mice, 78 sessions; PPC-A: 9 mice, 40 sessions; Wilcoxon Rank Sum test; mice and session number are the same for the following figures; Supplementary Table 1).

Figure 3. Tone-texture mismatch alters neuronal tuning to texture. (**a**) Average normalized spike rate of texture 2 discriminative neurons in S1, PPC-RL and PPC-A, in matched and mismatched trials. The spike rate of each neuron was normalized to be between 0 and 1 within each session. (**b**) The mean response amplitudes of all texture discriminative neurons in the texture window. Plots are shown across areas (rows) and trial types (columns). Each dot represents the responses of one neuron in one imaging session. (**c**) Selectivity index of the texture discriminative neurons during texture window, in different trial types. Selectivity index was calculated as the difference between the average response to the preferred texture and the average response to the non-preferred texture. (S1 1486 neurons; PPC-A 400 neurons; PPC-RL 618 neurons; Wilcoxon Rank-Sum test; Supplementary Table 1)

Figure 4. Tone-texture mismatch alters texture encoding in S1 and PPC populations. (**a**) Left: scheme of the decoders. Black line represents the decoder hyperplane; yellow and teal dots represent the neuronal population activity at a given time point in the trial; each dot was projected onto the orthogonal axis of the decoder hyperplane to represent the decoder confidence. Right: example procedure for texture decoding. (**b**) Neuronal population decoding of tone (top) and texture (bottom). Sensory encoding is represented by projection strength on the axes of linear decoders trained to discriminate tone and texture, in the tone and texture window, respectively. Line colors indicate area identity (magenta: S1; green: PPC-A; blue: PPC-RL); solid and dash lines indicate stimulus identity in the trial. (**c**) Discrimination index (DI) of tone decoder in the tone window. Stars above each box indicate significance compared to shuffled data (gray bars), for which

neurons identities were shuffled, while trial and time correspondences were kept the same. Stars across boxes indicate comparison between trial types. (**d**) DI of tone decoder in texture window. (**e**) DI of texture decoder in texture window. (**f**) Decoder projection strength of tone (top row) and texture (bottom row) in single-modality experiments. (**g**) DI of tone decoder and texture decoder in single-modality experiments, in tone window and texture window, separately. Stars represented as in (c). (S1: 14 mice, 118 sessions; PPC-RL: 14 mice, 78 sessions; PPC-A: 9 mice, 40 sessions; Wilcoxon Rank Sum test was used for comparison with shuffled data, Wilcoxon Signed-Rank test for comparison between trial types; Supplementary Table 1)

Figure 5. Interaction pattern of S1 and PPC areas during the behavioral task. (**a**) Illustration of canonical correlation analysis (CCA). The activity of each neuronal population can be represented as points in a high-dimensional space, where each dimension represents the activity of one neuron in this population. At a given time point in the trial, CCA identifies a set of canonical dimensions through linear combinations of variables from the two populations that have maximum correlation. (**b**) Illustration of defining separate CCA axes over the trial time. (**c**) Top canonical correlation between S1 and PPC-A (green), and S1 and PPC-RL (blue). Light colors indicate shuffled correlation, where only the trial correspondence between the two areas were shuffled, while trial structure was kept the same. (**d**) Average canonical correlation strength of (c) in each task window. (**e**) Number of significant interaction dimensions were determined by generating shuffled correlations and defining a threshold (mean + 3 S.D.) using the first correlation values. Canonical dimensions in real data with correlations higher than this threshold were considered significant. Example is from one imaging session. (**f**) Number of significant dimensions in S1 and PPC-A, and S1 and PPC-RL pairs. (**g**) Average number of significant dimensions of (f) in each task window. (S1↔PPC-A: 9 mice, 40 sessions; S1↔PPC-RL: 13 mice, 71 sessions; Wilcoxon Rank Sum test; Supplementary Table 1)

Figure 6. Top-down and bottom-up interactions between S1 and PPC areas during prediction mismatches. (**a**) Top-down interaction strength (PPC-A/RL to S1) was calculated by the average canonical correlation with a negative lag for PPC, and bottom-up interaction strength was calculated by the average correlation with a negative lag for S1 (left and middle panels). The direction and strength of S1-PPC interaction was characterized by the information flow index (IFI), defined as ratio of the difference between the two interactions to their sum (right panel). (**b**) Lagged canonical correlation between S1 and PPC-A, averaged across all sessions, for different trial types. (**c**) Information flow index computed from (b). (**d**) Quantification of information flow index between S1 and PPC-A. (**e**) Lagged canonical correlation between S1 and PPC-RL, averaged across all sessions, for different trial types. (**f**) Information flow index computed from (e). (**g**) Quantification of information flow index between S1 and PPC-RL. (S1↔PPC-A: 9 mice, 40 sessions; S1↔PPC-RL: 13 mice, 71 sessions; Wilcoxon Signed-Rank test; Supplementary Table 1)

Figure 7. A model of S1, PPC-A, and PPC-RL interactions during the behavioral task. (**a**) In the correct trials, tone information is encoded in PPC-A, potentially through inputs from auditory cortex (A1). PPC-A generates and communicate texture prediction with S1. During the texture presentation, S1 sends texture

information to PPC-A, while all three areas are involved in the processing and transformation of texture information. The decision is formed through coordinated efforts from S1 and PPC. (**b**) In mismatch-choose-texture trials, mice are in a state that attends more to S1 inputs. Texture information in S1 is sent to PPC-A, and choice is made according to actual texture. (**c**) In mismatch-choose-tone trials, tone induces strong texture prediction in PPC-A, which is sent to S1 during the tone and texture windows, overwriting the actual texture information in S1. Choice is made according to the predicted texture. Solid arrows represent directional interactions between recorded areas, dashed arrows represent putative interactions between pairs of areas that were not recorded simultaneously in this study.

References

1. Keller, G. B. & Mrsic-Flogel, T. D. Predictive Processing: A Canonical Cortical Computation. *Neuron* **100**, 424–435 (2018).

2. Norman, K. J. *et al.* Post-error recruitment of frontal sensory cortical projections promotes attention in mice. *Neuron* **0**, (2021).

3. Pakan, J. M. P., Currie, S. P., Fischer, L. & Rochefort, N. L. The Impact of Visual Cues, Reward, and Motor Feedback on the Representation of Behaviorally Relevant Spatial Locations in Primary Visual Cortex. *Cell Rep.* **24**, 2521–2528 (2018).

4. Schultz, W. & Dickinson, A. Neuronal Coding of Prediction Errors. *Annu. Rev. Neurosci.* **23**, 473–500 (2000).

5. Starkweather, C. K., Gershman, S. J. & Uchida, N. The Medial Prefrontal Cortex Shapes Dopamine Reward Prediction Errors under State Uncertainty. *Neuron* **98**, 616-629.e6 (2018).

6. Garner, A. R. & Keller, G. B. A cortical circuit for audio-visual predictions. *Nat. Neurosci. 2021 251* **25**, 98–105 (2021).

7. Fiser, A. *et al.* Experience-dependent spatial expectations in mouse visual cortex. *Nat. Neurosci. 2016 1912* **19**, 1658–1664 (2016).

8. Samuelsen, C. L., Gardner, M. P. H. & Fontanini, A. Effects of Cue-Triggered Expectation on Cortical Processing of Taste. *Neuron* **74**, 410–422 (2012).

9. Zhang, S. *et al.* Long-range and local circuits for top-down modulation of visual cortex processing. *Science (80-.).* **345**, 660–665 (2014).

10. Libby, A. & Buschman, T. J. Rotational dynamics reduce interference between sensory and memory representations. *Nat. Neurosci.* **24**, 715–726 (2021).

11. Schmack, K., Bosc, M., Ott, T., Sturgill, J. F. & Kepecs, A. Striatal dopamine mediates hallucination-like perception in mice. *Science (80-.).* **372**, (2021).

12. Corlett, P. R. *et al.* Hallucinations and Strong Priors. *Trends Cogn. Sci.* **23**, 114–127 (2019).

13. Gilday, O. D. & Mizrahi, A. Learning-Induced Odor Modulation of Neuronal Activity in Auditory Cortex. *J. Neurosci.* **43**, 1375–1386 (2023).

14. Kwon, S. E., Yang, H., Minamisawa, G. & O'Connor, D. H. Sensory and decision-related activity propagate in a cortical feedback loop during touch perception. *Nat. Neurosci. 2016 199* **19**, 1243–1249 (2016).

15. Semedo, J. D., Zandvakili, A., Machens, C. K., Yu, B. M. & Kohn, A. Cortical Areas Interact through a Communication Subspace. *Neuron* **102**, 249-259.e4 (2019).

16. Semedo, J. D. *et al.* Feedforward and feedback interactions between visual cortical areas use different population activity patterns. *Nat. Commun. 2022 131* **13**, 1–14 (2022).

17. Ebrahimi, S. *et al.* Emergent reliability in sensory cortical coding and inter-area communication. *Nat. 2022 6057911* **605**, 713–721 (2022).

18. Javadzadeh, M. & Hofer, S. B. Dynamic causal communication channels between neocortical areas. *Neuron* 2470-2483.e7 (2022).

19. Veuthey, T. L., Derosier, K., Kondapavulur, S. & Ganguly, K. Single-trial cross-area neural population dynamics during long-term skill learning. *Nat. Commun.* **11**, 1–15 (2020).

20. Campo, A. T. *et al.* Feed-forward information and zero-lag synchronization in the sensory thalamocortical circuit are modulated during stimulus perception. *Proc. Natl. Acad. Sci. U. S. A.* **116**, 7513–7522 (2019).

21. Chen, J. L. *et al.* Pathway-specific reorganization of projection neurons in somatosensory cortex during learning. *Nat. Neurosci.* **18**, 1101–1108 (2015).

22. Lyamzin, D. & Benucci, A. The mouse posterior parietal cortex: Anatomy and functions. *Neurosci. Res.* **140**, 14–22 (2019).

23. Song, Y. H. *et al.* A Neural Circuit for Auditory Dominance over Visual Perception. *Neuron* **93**, 940-954.e6 (2017).

24. Mohan, H. *et al.* Sensory representation of an auditory cued tactile stimulus in the posterior parietal cortex of the mouse. *Sci. Rep.* **8**, 1–13 (2018).

25. Raposo, D., Kaufman, M. T. & Churchland, A. K. A category-free neural population supports evolving demands during decision-making. *Nat. Neurosci. 2014 1712* **17**, 1784–1792 (2014).

26. Gallero-Salas, Y. *et al.* Sensory and Behavioral Components of Neocortical Signal Flow in Discrimination Tasks with Short-Term Memory. *Neuron* **109**, 1–14 (2020).

27. Gilad, A. & Helmchen, F. Spatiotemporal refinement of signal flow through association cortex during learning. *Nat. Commun. 2020 111* **11**, 1–14 (2020).

28. Gilad, A., Gallero-Salas, Y., Groos, D. & Helmchen, F. Behavioral Strategy Determines Frontal or Posterior Location of Short-Term Memory in Neocortex. *Neuron* **99**, 814-828.e7 (2018).

29. Pho, G. N., Goard, M. J., Woodson, J., Crawford, B. & Sur, M. Task-dependent representations of stimulus and choice in mouse parietal cortex. *Nat. Commun.* **9**, (2018).

30. Rindner, D. J., Proddutur, A. & Lur, G. Cell-type-specific integration of feedforward and feedback synaptic inputs in the posterior parietal cortex. *Neuron* **0**, (2022).

31. Park, I. M., Meister, M. L. R., Huk, A. C. & Pillow, J. W. Encoding and decoding in parietal cortex during sensorimotor decision-making. *Nat. Neurosci.* **17**, 1395–1403 (2014).

32. Chen, J. L., Voigt, F. F., Javadzadeh, M., Krueppel, R. & Helmchen, F. Long-range population dynamics of anatomically defined neocortical networks. *Elife* **5**, (2016).

33. Zhuang, J. *et al.* An extended retinotopic map of mouse cortex. *Elife* **6**, (2017).

34. Pachitariu, M. *et al.* Suite2p: beyond 10,000 neurons with standard two-photon microscopy. *bioRxiv* (2017) doi:10.1101/061507.

35. Helmer, M. *et al.* On stability of Canonical Correlation Analysis and Partial Least Squares with application to brain-behavior associations. *bioRxiv* (2021) doi:10.1101/2020.08.25.265546.

36. Audette, N. J., Zhou, W., Chioma, A. La & Schneider, D. M. Precise movement-based predictions in the mouse auditory cortex. *Curr. Biol.* **0**, (2022).

37. Hamm, J. P., Shymkiv, Y., Han, S., Yang, W. & Yuste, R. Cortical ensembles selective for context. *Proc. Natl. Acad. Sci.* **118**, e2026179118 (2021).

38. Parras, G. G. *et al.* Neurons along the auditory pathway exhibit a hierarchical organization of prediction error. *Nat. Commun. 2017 81* **8**, 1–17 (2017).

39. Hyman, J. M., Holroyd, C. B. & Seamans, J. K. A Novel Neural Prediction Error Found in Anterior Cingulate Cortex Ensembles. *Neuron* **95**, 447-456.e3 (2017).

40. Rodgers, C. C. & DeWeese, M. R. Neural Correlates of Task Switching in Prefrontal Cortex and Primary Auditory Cortex in a Novel Stimulus Selection Task for Rodents. *Neuron* **82**, 1157–1170 (2014).

41. Srinath, R., Ruff, D. A. & Cohen, M. R. Attention improves information flow between neuronal populations without changing the communication subspace. *Curr. Biol.* **0**, (2021).

42. Olcese, U., Iurilli, G. & Medini, P. Cellular and synaptic architecture of multisensory integration in the mouse neocortex. *Neuron* **79**, 579–593 (2013).

43. Hamm, J. P. & Yuste, R. Somatostatin Interneurons Control a Key Component of Mismatch Negativity in Mouse Visual Cortex. *Cell Rep.* **16**, 597–604 (2016).

44. Schulz, A., Miehl, C., Berry, M. J. & Gjorgjieva, J. The generation of cortical novelty responses through inhibitory plasticity. *Elife* **10**, (2021).

45. Harris, J. A. *et al.* Hierarchical organization of cortical and thalamic connectivity. *Nature* **575**, 195–202 (2019).

46. Deneux, T. *et al.* Context-dependent signaling of coincident auditory and visual events in primary visual cortex. *Elife* **8**, (2019).

47. Van Derveer, A. B., Ross, J. M. & Hamm, J. P. Robust multisensory deviance detection in the mouse parietal associative area. (2023) doi:10.1016/j.cub.2023.08.002.

48. Gilissen, S. R. J., Farrow, K., Bonin, V. & Arckens, L. Reconsidering the Border between the Visual and Posterior Parietal Cortex of Mice. *Cereb. Cortex* **31**, 1675–1692 (2021).

49. Zingg, B. *et al.* Neural networks of the mouse neocortex. *Cell* **156**, 1096–1111 (2014).

50. Goard, M. J., Pho, G. N., Woodson, J. & Sur, M. Distinct roles of visual, parietal, and frontal motor cortices in memory-guided sensorimotor decisions. *Elife* **5**, (2016).

51. Zhong, L. *et al.* Causal contributions of parietal cortex to perceptual decision-making during stimulus categorization. *Nat. Neurosci.* **22**, 963–973 (2019).

52. Oude Lohuis, M. N., Marchesi, P., Pennartz, C. M. A. & Olcese, U. Functional (ir)Relevance of Posterior Parietal Cortex during Audiovisual Change Detection. *J. Neurosci.* **42**, 5229–5245 (2022).

53. Driscoll, L. N., Pettit, N. L., Minderer, M., Chettih, S. N. & Harvey, C. D. Dynamic Reorganization of Neuronal Activity Patterns in Parietal Cortex. *Cell* **170**, 986-999.e16 (2017).

54. Morcos, A. S. & Harvey, C. D. History-dependent variability in population dynamics during evidence accumulation in cortex. *Nat. Neurosci.* **19**, 1672–1681 (2016).

55. Harvey, C. D., Coen, P. & Tank, D. W. Choice-specific sequences in parietal cortex during a virtual-navigation decision task. *Nature* **484**, 62–68 (2012).

56. Kira, S., Safaai, H., Morcos, A. S., Panzeri, S. & Harvey, C. D. A distributed and efficient population code of mixed selectivity neurons for flexible navigation decisions. *Nat. Commun. 2023 141* **14**, 1–28 (2023).

Methods

All procedures of animal experimentation were carried out according to the guidelines of the Veterinary Office of Switzerland and following approval by the Cantonal Veterinary Office in Zurich (licenses 234/2018, 211/2018).

Mice and dataset

Mice were housed on a 12-h reversed light/dark cycle at an ambient temperature of between 21 °C and 23 °C and humidity between 55% and 60%. 16 mice were included in this study. Mice were one of the following strains: RasGRF2a-dCre;CamK2a-tTA;TITL-GCaMP6f (M10, M11, M12, M25, M26, M28, M29, M33, M34, M35), GP5.17(C57BL/6J-Tg(Thy1-GCaMP6f)GP5.17Dkim/J, Jackson Laboratory 025393) (M14, M15), Snap25-IRES2-Cre-D;CamK2a-tTA;TITL-GCaMP6f (M17), RasGRF2a-dCre;tTA2-GCaMP6f (M30, M38, M40). All transgenic strains express GCaMP6f in layer 2/3 pyramidal neurons of the neocortex. Both sexes were included in this study (male: M10, M14, M15, M25, M26, M30, M33, M34, M35; female: M11, M12, M13, M17, M28, M29, M38, M40). All mice were adults (12-16 weeks old) when experiment started. Out of the 16 mice, S1-PPC$_A$ imaging was performed on 9 mice (M25, M26, M28, M29, M30, M33, M34, M35, M40); S1-PPC$_{RL}$ imaging was performed on 14 mice (M10, M11, M12, M14, M17, M25, M26, M28, M29, M30, M33, M34, M35, M40). Two mice (M15, M38) were only included in behavioral studies but not in the neuronal data analysis due to the decayed cranial window quality. One mouse (M17) was removed from cross-area analysis due to decayed S1 imaging quality from lateral skull bone growth under the cranial window. Mice were 2.5-4 months old at the beginning of behavior training, and 3-5 months old at the time of experiment.

Surgical procedures

A craniotomy was performed on all mice over S1 and PPC in the left hemisphere. Mice were anesthetized with 2% isoflurane mixed with oxygen, and body temperature was maintained at 37℃. After analgesia treatment (Metacam, 5 mg/kg, s.c.; lidocaine gel over the skull skin), the skull was exposed, a 4 mm round cranial window was made with dental drill, and covered with glass coverslip using dental cement (Tetric EvoFlow). A light-weighted head-bar was fixed on the skull using dental cement. After the surgery, animals were continually monitored for at least three days, and treated with analgesics (Metacam, 5 mg/kg, s.c.). For strains that expressed destabilized Cre (dCre), we induced stable GCaMP6f expression by administering trimethoprim (TMP, Sigma T7883). TMP was reconstituted in Dimethyl sulfoxide (DMSO, Sigma 34869) at a saturation level of 100 mg/ml, and intraperitoneally injected (150 mg TMP/g body weight; 29 g needle) at least one week before imaging commenced.

Behavior training

Mice were allowed to recover for at least 1 week before behavior training started. Mice were first accustomed to the hands of the experimenter at the home cage for several days until showing no sign of stress, then accustomed to head fixation. Then, mice were put under water scheduling, and were introduced to the behavior setup. During the first 2-3 sessions, mice were given sugar water reward from one of the two lick ports after the choice tone (2 beeps at 3 kHz of 50-ms duration with 50-ms interval). Once they learned to lick after the choice tone to obtain the water reward, we introduced the textures. Textures were followed by reward delivery on the corresponding lick port upon licking, and licks on the wrong port did not result in punishment or trial abort. This stage lasted for 1-2 sessions. Once mice were accustomed to the trial structure, we started formal training.

Behavior training was carried out using a custom written LabView software. Each trial started with one of two distinct auditory tones (10 kHz or 18 kHz, 6 repetitions, 50-ms duration and 50-ms intervals). One second after tone onset, the presentation of one of two distinct textures followed (sandpaper, P100 vs. P1200 for M10-17, P280 vs. P800 for M25-40). A rotary motor "swung" the texture onto the whisker pad from the top. The texture was presented for 1 second and then moved away from the mouse with a linear motor stage. At the end of the texture window, choice window started, indicated by the choice tone described above. The choice window lasted for up to 2 seconds. As soon as mice licked during the choice window, choice window was terminated and the reward window started. If mice choose the correct lick port, a small water reward was delivered (~4 µl sugar water); wrong choices were not punished. The inter-trial interval was randomly distributed between 4-8 seconds.

During training, when a mouse made incorrect choices, the same tone-texture stimulus pair was presented again in the following trial until the mouse chose correctly. This "repeat incorrect" strategy facilitates learning and prevents the mice from forming a bias towards one of the two lick ports. If the mouse disengages from licking, in 10% of these miss trials the reward was delivered after the choice window to motivate the mouse. Each day, the training lasted as long as the mouse was actively engaged in the task, typically 200-400 trials. Training was done once per day, 5-6 days per week. Weight, health, and water intake were monitored daily. All training was performed in the dark and monitored through a behavior camera with a small infrared light source. Mice were considered experts when they reached 75% correct performance for three sessions. Among all mice, three mice showed an unstable behavior, with relatively high fluctuations of the within-session performance (Extended Data Fig. 1a); however, they all showed clear signs of learning, reaching sub-session performance peaks above expert level for consecutive days. We attributed the unstable behavior to environmental stress; in particular, the training of M40 coincided with construction work in the animal facility, resulting in longer training duration.

Mismatched trial design

After mice became stable experts, we started introducing mismatched trials. In these sessions, the first 20-30 trials were with matched stimuli (without mismatch), and only afterwards mismatch trials were randomly

presented in 10%-30% of the trials. To avoid confusion for mice and prevent re-learning of new rules, we kept the repeat incorrect strategy throughout these sessions for matched trials, reinforcing the learnt rules. Because the task is mostly a texture-dependent task (see Results section, Fig. 1, and Extended Data Fig. 1), we rewarded according to the tone in mismatched trials, in order to encourage mice to pay attention to the tone and generate more mismatch-choose-tone response.

Single sensory modality experiments

Tone-only and texture-only sessions were done at the end of the experiment, after mice completed all mismatched sessions (7-12 sessions). In tone-only sessions, trials started with a 1-s auditory tone, as for the matched pairing condition. Afterwards, the rotary motor carrying the texture swung in, generating the same motor noise, but stopped above the whisker pad of mice. Therefore, texture was "presented" above the mice, out of reach for their whiskers. Choice window, reward window and inter-trial interval were the same as in matched condition. In texture-only sessions, the tone before the texture presentation was omitted. Trial started with a 1-s window with no sensory stimulus, followed by normal texture presentation, and then choice and reward windows. These single modality sessions typically were restricted to 100-150 trials to prevent re-learning.

After the single-modality experiments, we trimmed the whiskers of the mice, and conducted another texture-only session. This session served as a control experiment to exclude the possibility that mice relied on other environmental cues (visual, olfactory, etc.) to perform the task.

Behavior monitoring

Face and body movements as well as the pupil diameter of the mice were monitored and recorded using a CMOS infrared-sensitive camera (Basler acA1440-220um). A small 940-nm infrared LED was positioned in front of the mice to illuminate their face and body. Since mice were in complete darkness, their pupils were dilated by default. To monitor the pupil diameter with a larger dynamic range, we restrained the pupil by carefully positioning a small UV LED (385 nm, Thorlabs LED385L) close to the eye contralateral to the texture presentation. Trial-related behavior was recorded at 50 Hz, simultaneously with calcium imaging, triggered by each trial start. Licking was recorded throughout tone, texture, and choice windows, and was estimated based on the event rate from the capacitive lick sensor sampled at 100 Hz.

To extract body and face movements, we manually selected two regions of interest (ROIs), one on the whisker pad, the other on the forelimb and chest region. Movement was calculated as frame-to-frame variation by computing (1-corr(f_t, f_{t+1})), where corr(f_t, f_{t+1}) denotes the frame-to-frame correlation of the ROI. We tracked the pupil diameter using a custom MATLAB script: we first manually selected an ROI over the eye region, then binarized the pupil (pupil was bright due to two-photon illumination of the cortex at 920 nm). Then, pupil diameter was estimated by fitting the binary region to an ellipse. Body and face movements, as well as pupil diameter, were smoothed with a median filter of 200-ms width.

Sensory mapping

To determine the exact locations of S1 and PPC, we performed widefield sensory mapping on all the mice before the two-photon imaging sessions started, following a previously described procedure[26]. Mice were lightly anesthetized under 1% isoflurane and kept at 37℃. Three types of sensory stimuli were delivered: visual, whisker, and hindlimb. For visual stimulation, a small blue LED was positioned close to the eye contralateral to the cranial window, and a brief 200-ms flash was presented, followed by 10-s recovery time. For whisker and hindlimb stimulation, a loud speaker-coupled vibrating bar was used to induce a vibrating touches of the whiskers and hindlimb paw (20 Hz for 2 s) on the side contralateral to the cranial window. Each stimulus modality was repeated 30 times.

Widefield imaging was simultaneously performed through the cranial window. A blue LED light source (Thorlabs; M470L3) was used for excitation of GCaMP6f, together with an excitation filter (480/40 nm BrightLine HC). The excitation light was directed through a dichroic mirror (510 nm; AHF; Beamsplitter T510LPXRXT) to a 4x objective (Thorlabs TL4X-SAP, NA 0.2). Emission light was filtered (emission filter 529/24 nm, BrightLine HC), and passed through the dichroic mirror to separate emission light with excitation light, then through a tube lens (Thorlabs TTL100-A) onto a sensitive CMOS camera (Hamamatsu Orca Flash 4.0).

To obtain a more precise location of PPC-RL and PPC-A, we further generated a retinotopic map through visual field sign mapping, following a previously described procedure[33]. Briefly, a drifting spherically-corrected checkerboard visual stimulus was presented on an LED screen (Adafruit Qualia 9.7" DisplayPort Monitor, 2048x1536 Resolution) across the visual field of the mice at 0.043–0.048 Hz. The stimulus sequence consisted of four cardinal directions, each presented with 10 repetitions. The screen was positioned in front of the eye contralateral to the cranial window, such that the stimulus covered retinotopic locations from approximately -20 to +30 degrees in altitude and -10 to +90 degrees in azimuth. The retinotopic map was calculated using previously reported analysis pipeline[33]. The final location of S1, PPC-A and PPC-RL was determined by optimally aligning the sensory map and retinotopic map together to the Allen Mouse Common Coordinate[45].

Two-area two-photon imaging

Two-area two-photon imaging was performed using a custom-built microscope that has been previously reported[32]. The simultaneous two-area imaging was implemented through a temporal multiplexing technique, where the laser pulse train from a Ti:sapphire laser (Mai Tai HP DeepSee, Spectra-Physics) was split in two temporally interleaved copies, each directed through an independently movable unit to a separate field of view. Each beam path was equipped with an electrically tunable lens (Optotune EL-10-30-C) to enable rapid focal changes for imaging multiple depths. Imaging was done at 920-nm excitation with a green emission filter (510/42 nm bandpass). A 16x objective was used (N16XLWD, Nikon, NA 0.8). The microscope was

controlled by a custom-written software Scope (http://sourceforge.net). Calcium imaging was acquired at 3 different depths in layer 2/3, separated by 40-50 μm. The FOV size was ~450×500 μm, at a resolution of ~370×256 pixels. The volume rate was typically ~9.32 Hz for two areas and three imaging depths per area. Laser power was adjusted for each plane, at 40-70 mW under the objective. For each mouse, the FOV positions and/or depths were slightly adjusted for each imaging session to cover different neuronal populations in S1 and PPC. Imaging was triggered by the start of each trial, and the image acquisition finished 0.5 s before the end of the inter-trial interval (i.e., the start of the next trial). During the duration of the experiment, most mice maintained a clear window with good imaging quality. The number of imaging sessions for each mouse is as following: For S1-PPC_A imaging, the number of sessions was 3, 4, 5, 5, 4, 4, 7, 4, 4, for M25, M26, M28, M29, M30, M33, M34, M35, M40, respectively. For S1-PPC_{RL} imaging, the number of sessions was 10, 9, 10, 2, 1, 8, 5, 4, 8, 5, 3, 4, 4, 3, for M10, M11, M12, M14, M17, M25, M26, M28, M29, M30, M33, M34, M35, M40, respectively. Note that the number of PPC-RL sessions was higher for M10, M11 and M12 due to a lower percentage of mismatch trials (~10% mismatch trials).

Processing of two-photon imaging data

We used Suite2p to extract neuronal traces[34]. This pipeline includes a rigid motion correction on the raw data, a model-based background subtraction, a neuron-identification algorithm, fluorescence extraction, and a neuron classifier. Raw fluorescence and neuropil traces were extracted from identified neurons, and neuropil-corrected traces were obtained. A deconvolution algorithm was applied to the corrected fluorescence traces to estimate the spike rate of neurons (in arbitrary units). Spike rate was further normalized by the baseline F0 estimated by Suite2p. We tuned the neuron classifier in the above pipeline to identify potential neurons, and we further manually curated each dataset to discard non-neuronal structures or low-quality ROIs. All analysis was performed using deconvolved spike rates.

To exclude redundant neurons due to fluorescence signal bleed-through between two areas or between two neighboring depths, we removed neurons that were highly correlated neighboring neurons, using similar criteria as previously described[57]. We defined potential duplicated neuron pairs as: (1) spike rate correlation above 0.5; (2) lateral distance between centroids below 5 μm regardless of depths; (3) appeared in adjacent imaging depths in the same imaging area (signal bleed-through in the same area from adjacent imaging planes), or appeared in the same imaging depths in different imaging areas (signal bleed-through across areas from the same imaging plane). In these duplicated neuron pairs, we kept the neuron with highest average fluorescence level, and discarded the one with less fluorescence.

Due to the variable length of the choice window, we defined choice window as the 0.5-s time period before the lick that triggered reward window (equivalent to the 0.5-s period before the reward window). We resampled all behavior data to match the calcium imaging rate. Due to slight differences in imaging rate (caused by slightly different pixel numbers), when combining datasets together, we resampled all dataset to a standard 10 Hz rate. These procedures were applied before all the analysis below.

Responsive neuron analysis

To identify neurons that are responsive to different task phases, we tested the activity level of individual neurons across task windows, for T_{tone}, $T_{texture}$, T_{choice}, and T_{reward}. We first denoised the deconvolved spike rates by a small Gaussian window (3 frames, sigma=1); then, for each neuron N_i and each task window T_j, we compared its average activity within the window, and generated a baseline distribution by randomly sampling the same number of frames outside of window T_j and computing average activity, for 100 times. If the activity of neuron N_i in T_j was significantly higher than outside of T_j, determined by a one-tailed Wilcoxon Rank Sum test ($p<0.05$), then we define neuron N_i as responsive in task window T_j.

To identify neurons that are discriminative for a specific task variable (tone, texture, choice, and reward), we compared the activity of responsive neurons as defined above for the different values of the task variables. For each task variable (for example texture), there are two potential values s_1 and s_2 (for example, texture 1 and texture 2). We compared the average activity of each neuron within the corresponding task window (texture window in this example) between s_1 trials and s_2 trials, using Wilcoxon Rank Sum test. If the neuronal activity was significantly higher ($p<0.05$) in s_1 trials, then the neuron was defined as a discriminative neuron with preference for s_1. We performed this procedure for all the four task variables. Responsive and discriminative neurons identified with this method are non-random, as no significant neurons were identified in shuffled data, where the activity of individual neurons was randomized within sessions. The relatively low percentage of discriminative neurons is due to several factors: (1) We calculate percentage using all detected neurons from the entire imaged population (several hundreds of neurons using our custom microscope); (2) we defined discriminative neurons as a subset of responsive neurons, i.e., they were required to have increased firing rate during the specific task phase; (3) we used two relatively similar textures P280 and P800 in our task design.

Responsive neuron analysis with GLM

To further dissect texture- and choice-related activity during texture presentation, we built Gaussian GLM (with identity link function) with two regressors (texture and choice) to predict the average texture window activity of each neuron, following a previously published procedure[58]. Each regressor contains two values: -1 (texture 2 and choice 2) and 1 (texture 1 and choice 1). For each neuron, we trained a full model using all regressors with two-fold cross-validation. To avoid overfitting, we applied ridge regularization with a lambda penalty of 0.1. We quantified model performance by computing the correlation value between the predicted activity and real activity. To identify the contribution of each regressor, we shuffled each regressor vector 100 times while maintaining the rest unchanged, and fitted model as above. We considered a neuron to be texture- or choice-responsive if the correlation value of full model is 1.96 standard deviation away from the shuffled distribution. Among these neurons, discriminative neurons were identified as described in the section above.

Decoder analysis

We trained four types of linear support vector machine (SVM) decoders: tone, texture, choice, and reward decoders, respectively. Similar to the responsive neuron analysis, each type of decoder was trained with two class labels (texture 1 vs. texture 2, for example), using frame-concatenated spike rate data from the corresponding task window (texture window, for example). A separate decoder was trained for each imaging session and each area (S1, PPC-A, PPC-RL), due to different imaging populations. Only matched pairing trials were used for training decoders.

For each imaging session, we randomly divided all the matched pairing trials into 10 subsets. We trained 10 decoders by excluding one subset at one time, therefore each decoder was trained on 90% of the training set. To avoid overfitting, we regularized the SVM coefficients with ridge (L2) penalty. The regularization term was cross-validated in a log space of 10 parameters from 10^{-5} to 10^{1}. To avoid overfitting due to unbalanced class number, we also implemented a misclassification cost that is inversely correlated with the total number of each class. The projection strength of each trial was calculated using the decoder that was not trained using this trial. The projection strength at time t of a trial was defined as the dot product between the decoder coefficient (without the constant term) and the population spike rate vector at t. Shuffled controls were generated by randomizing the neuron identities in the dataset and applying the decoders to shuffled data. To evaluate the decoder performance, the ROC (receiver operating characteristic) curve and the AUC (area under curve) were calculated using standard approaches, and discrimination index (DI) was defined as (AUC-0.5)×2. DI=0 represents chance level; DI=1 represents perfect classification performance.

CCA analysis

To measure the optimal population correlation between cortical areas, we applied a previously reported method, the canonical correlation analysis (CCA)[16,19]. CCA identifies pairs of dimensions from the imaged neuronal populations in the two cortical areas, such that the correlation between the projected activities onto the dimension is maximized. Given the activity of two neuronal populations, a $n_x \times t$ matrix $\mathbf{X}$ from area 1, and a $n_y \times t$ matrix $\mathbf{Y}$, where t is the number of time points, and n_x and n_y are the number of neurons in each area, CCA identifies in total $\min(n_x,n_y)$ pairs of dimensions, and the projection correlation of these dimensions decreases from the first to last. Similar to principal component analysis (PCA), CCA finds a set of projection axes for each area; the difference is that PCA aims at maximizing the variance explained by top axes from $\mathbf{X}$ and $\mathbf{Y}$, independently, while CCA aims at maximizing the projection correlation between the activity matrices $\mathbf{X}$ and $\mathbf{Y}$.

CCA requires a sufficient amount of samples to generate stable solutions[35]. In our experiments, we typically imaged 200-300 neurons in each area, and we recorded 200-400 trials per session. A previous study using simulated datasets has shown that ~50 samples per variable is required to generate a stable solution[35]. To ensure such condition is met, we first performed PCA to reduce the dimensionality (number of variables) per area, keeping the first 30 principal components (PCs). Overall, the top 30 PCs captured a substantial part of the variance in the dataset (variance explained by 30 PCs: S1 55.0±1.2, PPC-A 59.9±1.4, PPC-RL 53.7±1.5

[mean±SEM]). We aimed at generating a separate CCA model at each time point over the trial time; to further increased the sample number, and to avoid outliers as well as to introduce certain temporal smoothness, we took a sliding time window of 0.5 s (5 frames) for training. Using a smaller time window (0.3 s) yielded more noisy but overall similar results (Supplementary Figure 1). For each time window, we randomly divided the data into 10 subsets, and generated 10 models by leaving one subset out each time. The final correlation is computed as the average from the 10 models.

The stimuli in the task result in co-activation of neurons caused by common inputs. As we were interested in the intrinsic interaction between cortical areas, we analyzed the residual activity by subtracting stimulus-triggered averages of PCs, from eight types of stimulus combination (2 tones, 2 textures, 2 choices). Additionally, we observed performance variability within individual sessions, and to ensure that we were analyzing trials during which mice were engaged in the task, we divided each session into sub-sessions of 20 trials, and used only the sub-sessions with performance rate above 75% for analysis. For tone-only and texture-only conditions, we kept the last 50 trials (out of 100-150 trials) when performance had stabilized. This resulted in 40-400 trials for each session.

Since we reduced the dimensionality of each population to its top 30 PCs, the CCA model generated 30 dimensions with descending inter-areal correlation. To determine the number of significant dimensions, we shuffled the trial correspondence between the two areas 100 times and computed the CCA correlations in the same way as above. Significance threshold was defined as mean + 3 S.D. (standard deviation) of the highest shuffled correlation. CCA dimensions with correlations exceeding the significance threshold were regarded as significant dimensions. Overall, we observed 1-2 significant dimensions across datasets and time points, therefore we focused on the first CCA dimension for analysis.

To analyze top-down and bottom-up interactions, we introduced a negative lag of up to 0.5 s with 0.1-s increment to each area, separately. For top-down interaction, we introduced a negative lag to the PPC data (PPC-A or PPC-RL); for bottom-up interaction, we introduced a negative lag to the S1 data. At each lag, we generated a CCA model, consisting of two separate loading matrices corresponding to the two areas. Then, for each trial type (correct, mismatch-choose-texture, and mismatch-choose-tone), we computed the projection correlation of all trials in this trial type. This approach avoided the potential instability of training the CCA model for each trial type, which does not guarantee enough sample numbers. From here, the lagged correlation map was slightly smoothed with a small Gaussian kernel (3 frames, sigma=1) to reduce noise between temporally consecutive models, and top-down and bottom-up interaction strengths were computed as the average CCA correlations across 0.3 s lags. Using different lags (0.1 s, 0.5 s) gave similar results as shown in Fig. 6. The direction and strength of information was quantified as information flow index (IFI), defined as (bottom-up – top-down)/(bottom-up + top-down). IFI is bounded between -1 and 1; values close to -1 represent top-down dominant information, values close to 1 represent bottom-up dominant information, whereas values close to 0 represent simultaneous or no information transfer.

Pearson correlation analysis

To verify our results of CCA, we also calculated population correlations using Pearson correlation instead of CCA. The imaging data were processed in the same way as for CCA analysis but population correlation was computed as the Pearson correlation between the flattened residual matrices of the two areas. Shuffled correlation was computed from trial-shuffled residual matrices. Unlike CCA, which found positive correlation in all cases, Pearson correlation resulted in negative values in some cases. For the calculation of IFI, we first normalized the lagged correlation map to be between 0 and 1, then calculated IFI for each trial type.

Statistics and Reproducibility

All statistical analysis was done in MATLAB. In general, Wilcoxon signed-rank test was used for paired samples, and Wilcoxon Rank Sum test was used for non-paired samples. No normality test was performed since these tests do not assume normality. Equal variance was assumed but not formally tested. Two-sided tests were performed unless otherwise indicated. No statistical methods were used to pre-determine sample sizes, but our sample sizes are similar to those reported in previous publications[10,26,59]. Error bars represent mean±SEM. Boxplots indicate the median (center line), 25% and 75% quartiles (box limits), and 1.5 × interquartile range (whiskers). The exact p-values are included in Supplementary Table 1. Mice were randomly assigned to imaging conditions (S1-A or S1-RL imaging) on each day. Stimulus presentation during imaging was fully randomized. Data collection and analysis were not performed blind to the conditions of the experiments.

Data availability

A subset of the data is available at a Zenodo repository[60] due to space limitation. The full dataset is available from the corresponding authors upon request.

Code availability

Example data processing and analysis code is available at a Zenodo repository[60].

Methods references

57. Han, S., Yang, W. & Yuste, R. Two-Color Volumetric Imaging of Neuronal Activity of Cortical Columns. *Cell Rep.* **27**, 2229-2240.e4 (2019).

58. Buetfering, C. *et al.* Behaviorally relevant decision coding in primary somatosensory cortex neurons. *Nat. Neurosci. 2022 259* **25**, 1225–1236 (2022).

59. Chen, J. L., Carta, S., Soldado-Magraner, J., Schneider, B. L. & Helmchen, F. Behaviour-dependent recruitment of long-range projection neurons in somatosensory cortex. *Nature* **499**, 336–340 (2013).

870 60. Han, S. Behavior-relevant top-down cross-modal predictions in mouse neocortex. *Zenodo* (2023) doi: 10.5281/zenodo.10078711.

Extended Data Figures

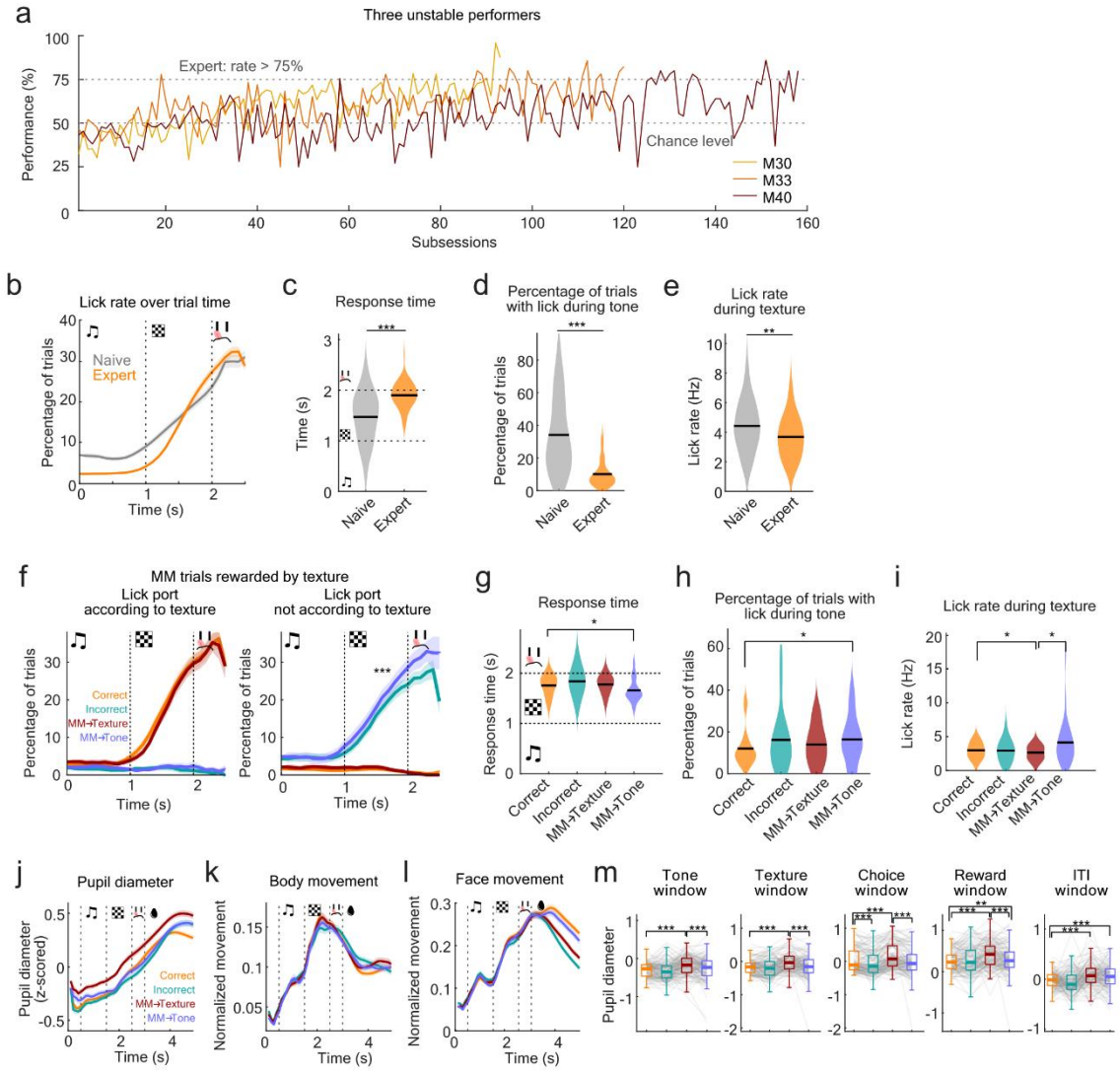

Extended Data Figure 1. Additional behavior analysis. (**a**) Each day, all the trials were split into 2-5 subsessions of 100-150 trials. Three unstable performer mice that did not reach expert threshold in daily average all showed expert performance in individual subsessions. (**b**) Lick rate over time for naïve and expert mice. (**c**) Response time of naive (performance<55%, 16 mice, 80 sessions) and expert mice (performance>75%, 13 mice, 74 sessions). (**d**) Percentage of trials with lick during tone on the lick port of final choice for naïve and expert mice. (**e**) Lick rate during texture for naïve and expert mice. (**f**) Lick probability over trial time on the lick ports according to texture identity (left) or the opposite lick port (right), during sessions where mismatched trials were rewarded according to texture (same for g-i). (**g**) Response time for different trial types. Mismatch-choose-tone condition shows a shorter response time overall (p = 0.0147). (**h**) Percentage of trials in each session, in which licks on the final choice spout were recorded during tone presentation (p=0.0186). (**i**) Lick rate during texture presentation for different trial types (p=0.0399, 0.0068). (**j**) z-scored pupil diameter in different trial types. (**k**) Body movement (normalized between 0 and 1 within each day) across trial types. (**l**) Face movement (normalized between 0 and 1 within each day) across trial types. (**m**) Statistics of pupil diameter across trial time. (***p<0.001, **p<0.01, *p<0.05, same for all following figures; (b-e): Wilcoxon Rank Sum test, (f-m): Wilcoxon signed-rank test; (a-e, j-m) mice and session numbers are the same as Fig. 1; (f-i) 6 mice, 17 sessions; Supplemental Table 1).

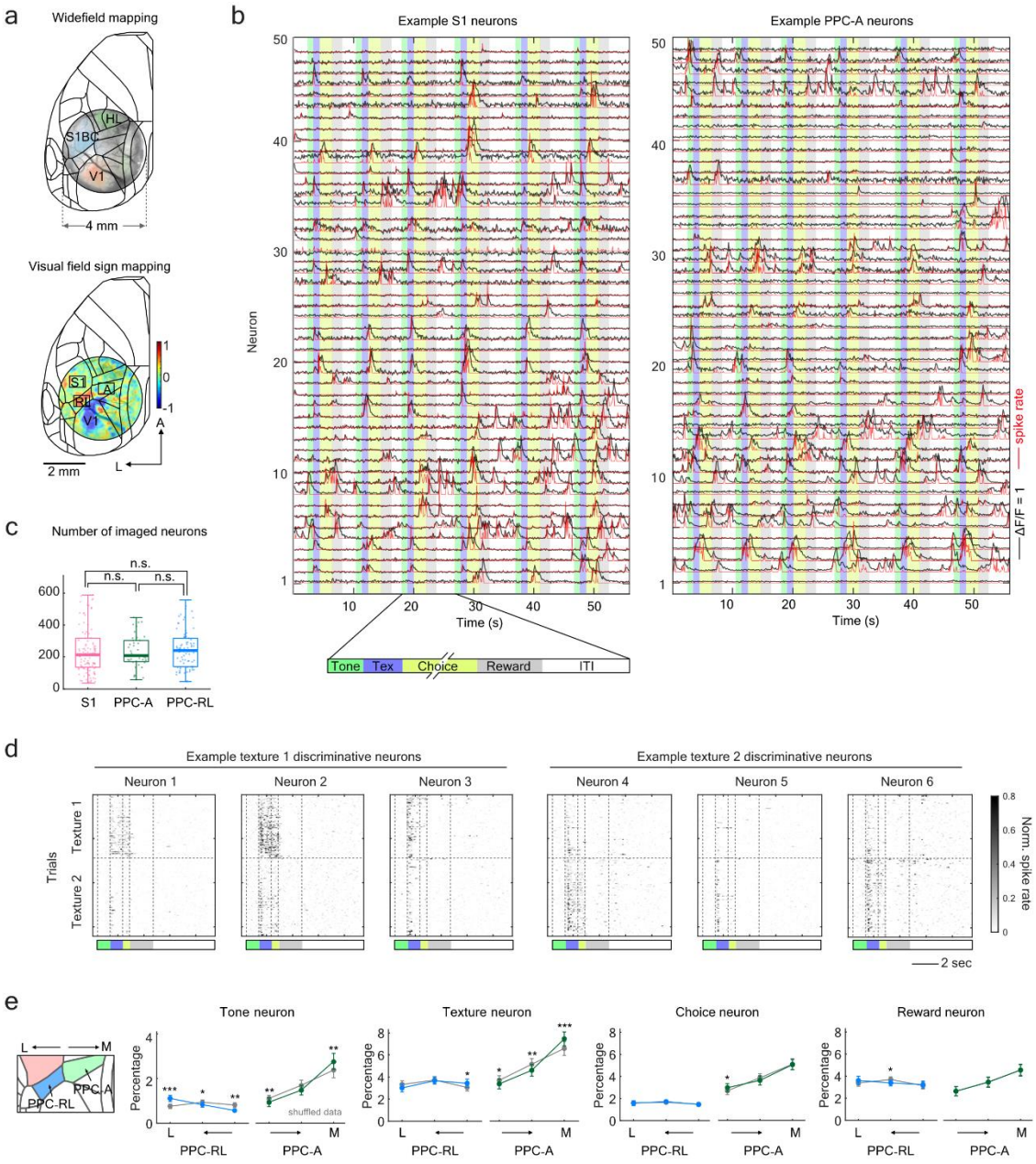

Extended Data Figure 2. Example traces and additional control experiment statistics. (**a**) The locations of S1, PPC-A and PPC-RL were determined by widefield sensory mapping using whisker, visual and hindlimb stimulation (top) under light anesthesia, as well as visual field sign mapping (bottom). (**b**) Example ΔF/F (black) and deconvolved spike rate (red) of two simultaneously imaged S1 and PPC-A populations. Due to space limitation, only 50 neurons are shown for each area. Colored stripes in the background indicate task windows. Some neurons were silent in the example time period shown in the plot. (**c**) Number of imaged neurons for each area are not significantly different. (**d**) Example single trial activities of texture discriminative neurons. Three example neurons from the same imaging session are shown for each texture preference; choice window was resampled to be the 0.5-s window before the reward window. Trial structure color code is the same as in (b). (**e**) Distribution of PPC task-responsive neurons along the medial-lateral (M-L) axis. Task-responsive neurons in PPC-RL and PPC-A were assigned to 3 spatial bins along the M-L axis. Percentage was calculated using the number of total neurons in each area. Shuffled data is represented in gray, where the neurons that the match number of responsive neurons were randomly drawn from the population. (Wilcoxon signed-rank test; Supplemental Table 1)

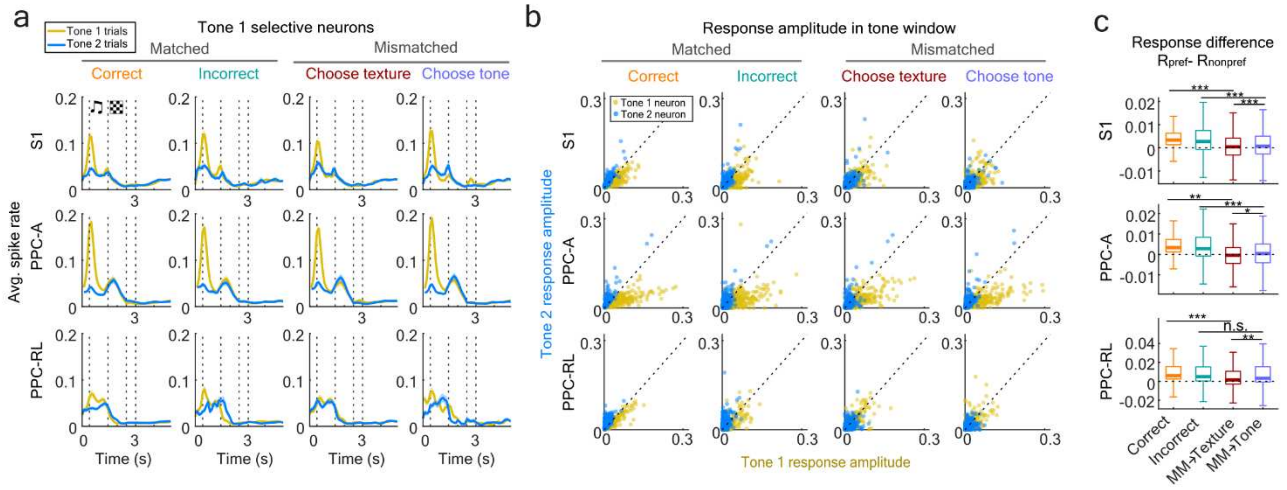

910 **Extended Data Figure 3. Response amplitude of tone-discriminative neurons.** (**a**) Averaged normalized spike rate of tone 1 discriminative neurons in S1, PPC-RL and PPC-A, in matched and mismatched trials. The spike rate of each neuron was normalized to be between 0 and 1 within each session. (**b**) Response amplitude to tone 1 and 2 of all tone discriminative neurons, during tone window, across areas and trial types. (**c**) Selectivity index of texture discriminative neurons during texture window, in different trial types. Significance 915 level was determined from shuffled data where the trial labels were shuffled. (Wilcoxon Rank Sum test; S1: 130 neurons; PPC-A: 179 neurons; PPC-RL: 105 neurons; Supplemental Table 1)

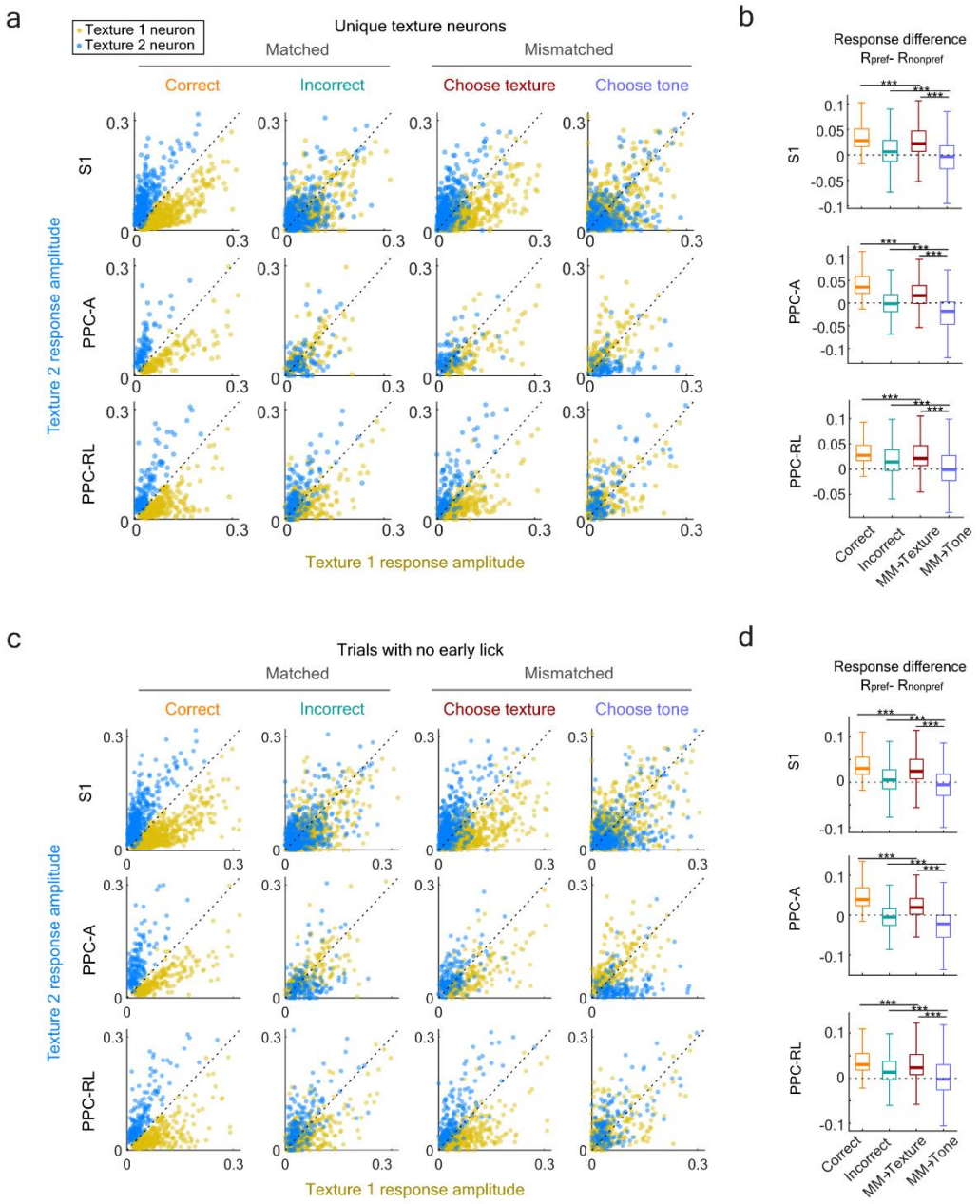

Extended Data Figure 4. Response amplitude of texture-discriminative neurons without the influence of choice. (**a**) Response amplitude to texture 1 and 2 of all texture discriminative neurons that were not choice-responsive, during texture window, across areas and trial types. Each dot represents the response of one neuron in one imaging session. (**b**) Selectivity index of texture discriminative neurons during texture window, in different trial types. Selectivity index was calculated as the difference between the average response to the preferred texture and the average response to the nonpreferred texture. (S1: 1275 neurons; PPC-A: 248 neurons; PPC-RL: 514 neurons). (**c**) Response amplitude to texture 1 and 2 of all texture discriminative neurons, in trials without early licks. (**d**) Selectivity index of neurons in (c). Neuron numbers in c-d are the same as in Fig. 3. (Wilcoxon Rank Sum test; Supplemental Table 1)

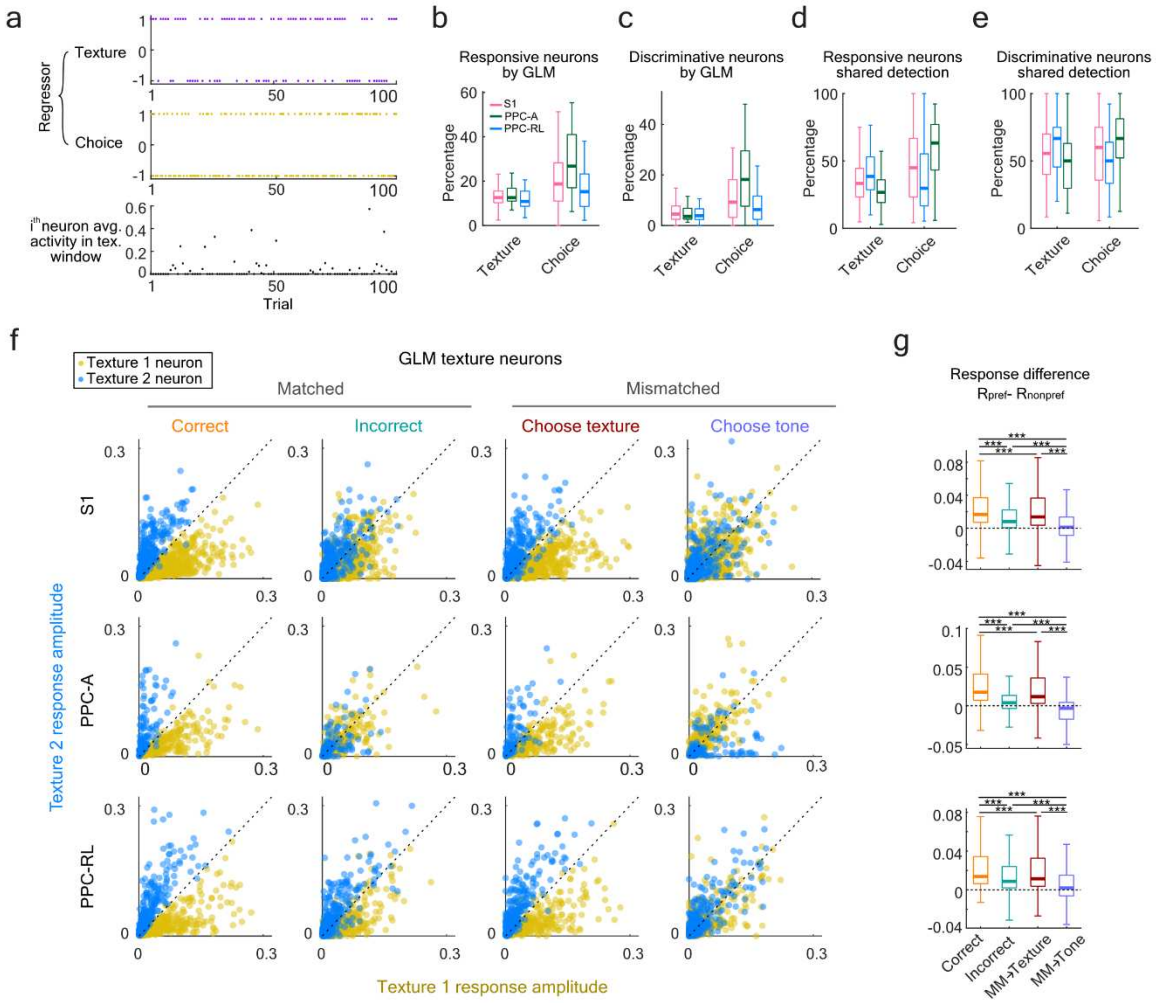

Extended Data Figure 5. Response amplitude of texture-discriminative neurons identified by GLM model. (**a**) Scheme of GLM regression. Two discrete regressors, texture and choice, were used to model the average activity during choice window, for each neuron. Regression performance was measured by the correlation value of predicted activity with real activity. Task responsive neurons were identified by comparing these correlation values against models generated by shuffling one regressor at a time. (**b**) Percentage of texture- and choice-responsive neurons identified by GLM from texture window. (**c**) Percentage of texture- and choice-discriminative neurons identified by GLM from texture window. (**d**) Percentage of task responsive neurons in Fig. 2d that are also identified by GLM method. (**e**) Percentage of task discriminative neurons in Fig. 2e that are also identified by GLM method. (**f**) Response amplitude to texture 1 and 2 of all GLM-identified texture discriminative neurons during texture window. Each dot represents the response of one neuron in one imaging session. (**g**) Selectivity index of texture discriminative neurons in (f). (Wilcoxon Rank Sum test; S1: 1478 neurons; PPC-A: 458 neurons; PPC-RL: 910 neurons; Supplemental Table 1)

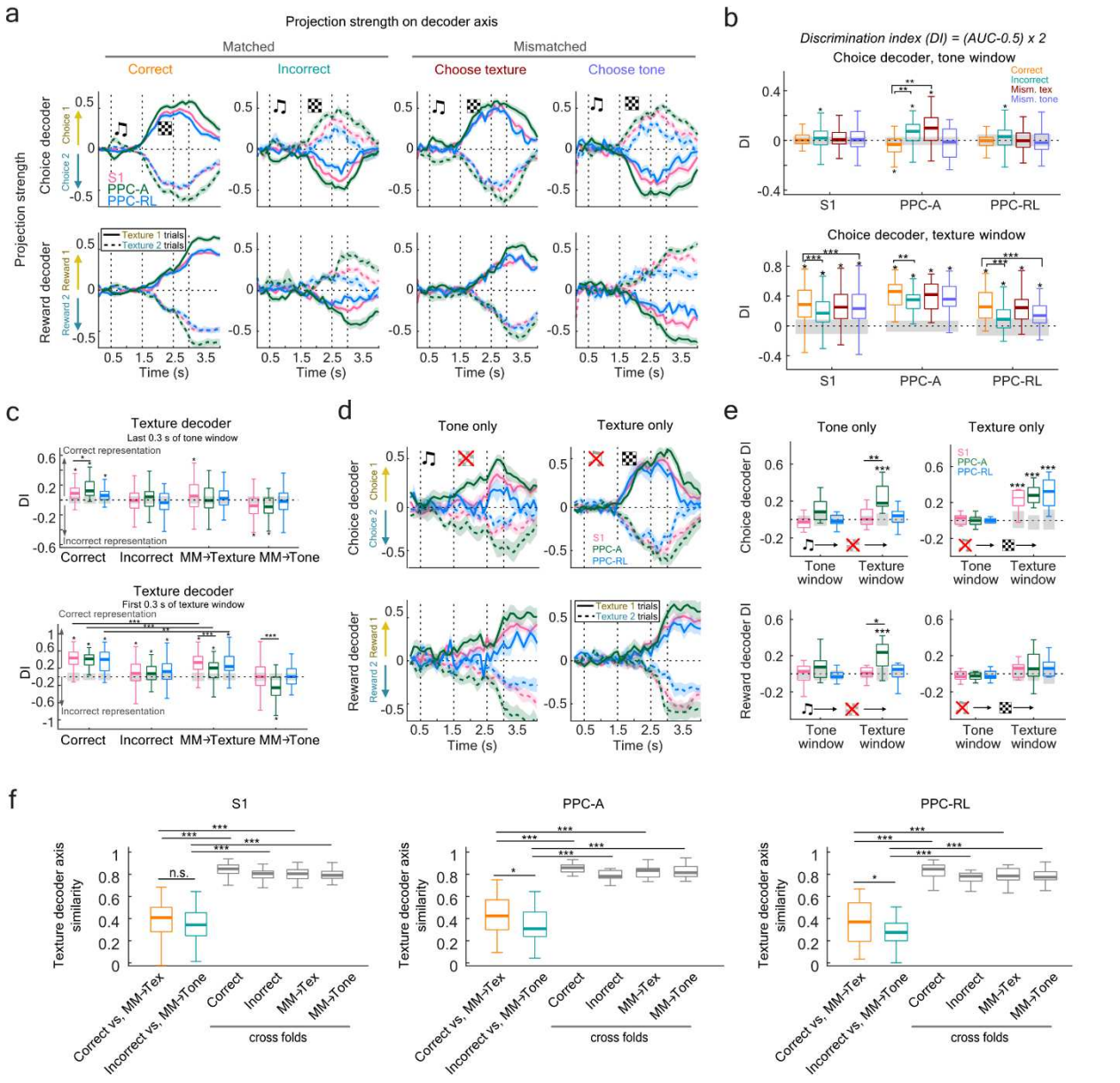

Extended Data Figure 6. Choice and reward encoding in S1 and PPC. (**a**) Neuronal population encoding of choice (top panels) and reward (bottom panels). Line colors indicate area identity; solid and dash lines indicate texture identity of the trial. (**b**) Discrimination index (DI) of the choice decoder and reward decoder, in the tone window and texture window, separately. Stars above each box indicate the significance with shuffled data (gray bars) where neurons identities were shuffled, while trial and time correspondence were kept the same. Stars across boxes indicate comparison between trial types. (**c**) DI of texture decoder before texture onset (last 0.3 s of tone window, top panel) and after texture onset (first 0.3 s of texture window, bottom panel). (**d**) Neuronal population encoding strength of choice (top panels) and reward (bottom panels) in single modality experiments. (**e**) DI of choice decoder and reward decoder in single modality experiments, in tone window and texture window, separately. (**f**) Texture decoder axis similarity (projection axis correlation) from decoders trained with each trial type, separately. For each trial type, trials was randomly split to two subsets, and two separate decoders were trained. The averaged axis were used for decoder similarity between trial types, and cross folds represent the similarity between two independent decoders trained with the same trial type. Sessions with less than 30 trials for each trial type were excluded to ensure enough training samples. (Supplemental Table 1)

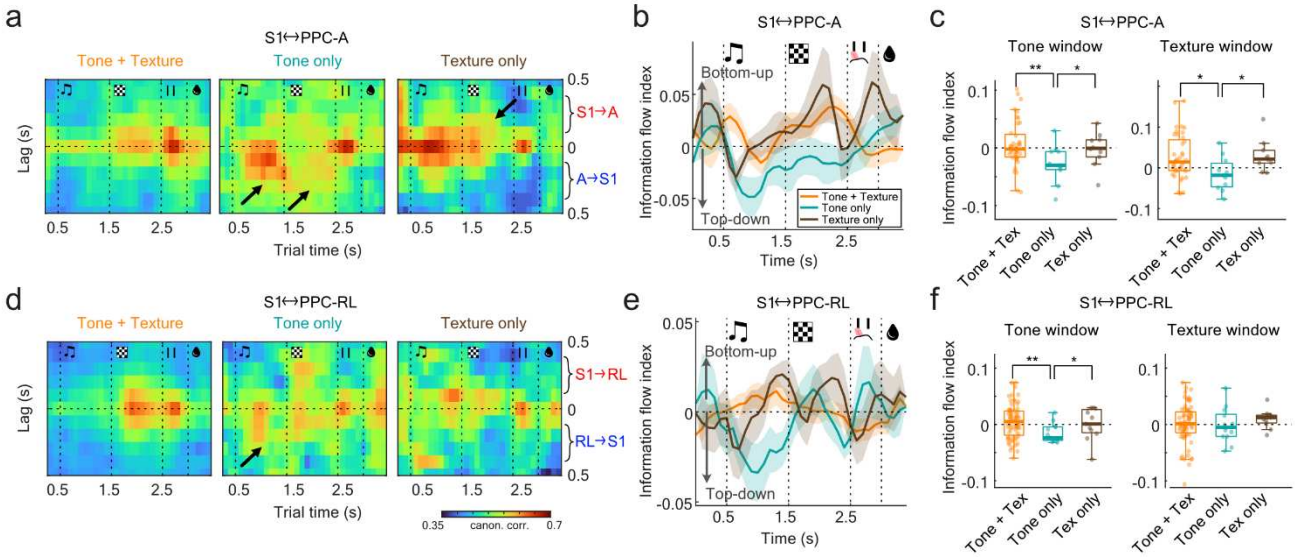

Extended Data Figure 7. Interaction between S1 and PPC in single modality trials. (**a**) Lagged canonical correlation between S1 and PPC-A averaged across all sessions, for matched stimuli (tone-texture), tone only, and texture only conditions. Note the stronger top-down (A to S1) interaction in tone only condition, and stronger bottom-up (S1 to A) interaction in texture only condition. (**b**) Information flow index quantified from (a). (**c**) Quantification of information flow index between S1 and PPC-A. (**d**) Averaged lagged canonical correlation between S1 and PPC-RL. Note the slightly stronger top-down (RL to S1) interaction during tone window in tone only condition. (**e**) Information flow index quantified from (d). (**f**) Quantification of information flow index between S1 and PPC-RL. (Wilcoxon Rank Sum test; Supplemental Table 1)

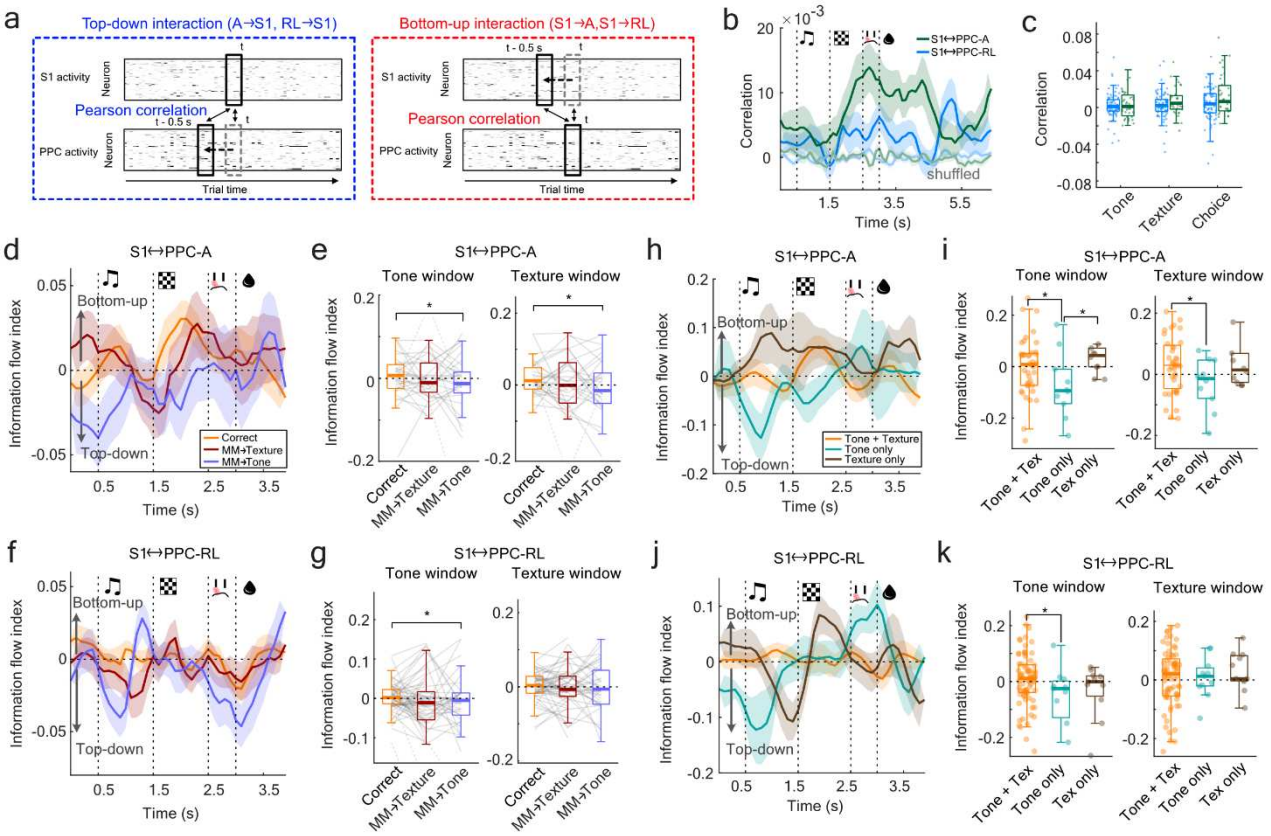

Extended Data Figure 8. Top-down and bottom-up interaction analysis with Pearson correlation. (**a**) Top-down and bottom-up interaction strength were evaluated in the same way as Fig. 6a, except that the correlation was calculated using Pearson correlation instead of CCA. (**b**) Population correlation between S1 and PPC-A (green), and S1 and PPC-RL (blue). (**c**) S1-PPC_A showed slightly stronger interaction than S1-PPC_{RL}. (**d**) Information flow index (IFI) of S1-PPC_A interaction using Pearson correlation. (**e**) Quantification of (d). (**f**) Information flow index of S1-PPC_{RL} interaction using Pearson correlation. (**g**) Quantification of (f). (**h**) Information flow index of S1-PPC_A interaction in single modality conditions. (**i**) Quantification of (h). Consistent with CCA analysis, tone only condition led to stronger top-down information flow during tone and texture windows. (**j**) Information flow index of S1-PPC_{RL} interaction in single modality conditions. (**k**) Quantification of (j). Consistent with CCA analysis, tone only condition led to stronger top-down information flow during tone. (Wilcoxon signed-rank test; Supplemental Table 1)

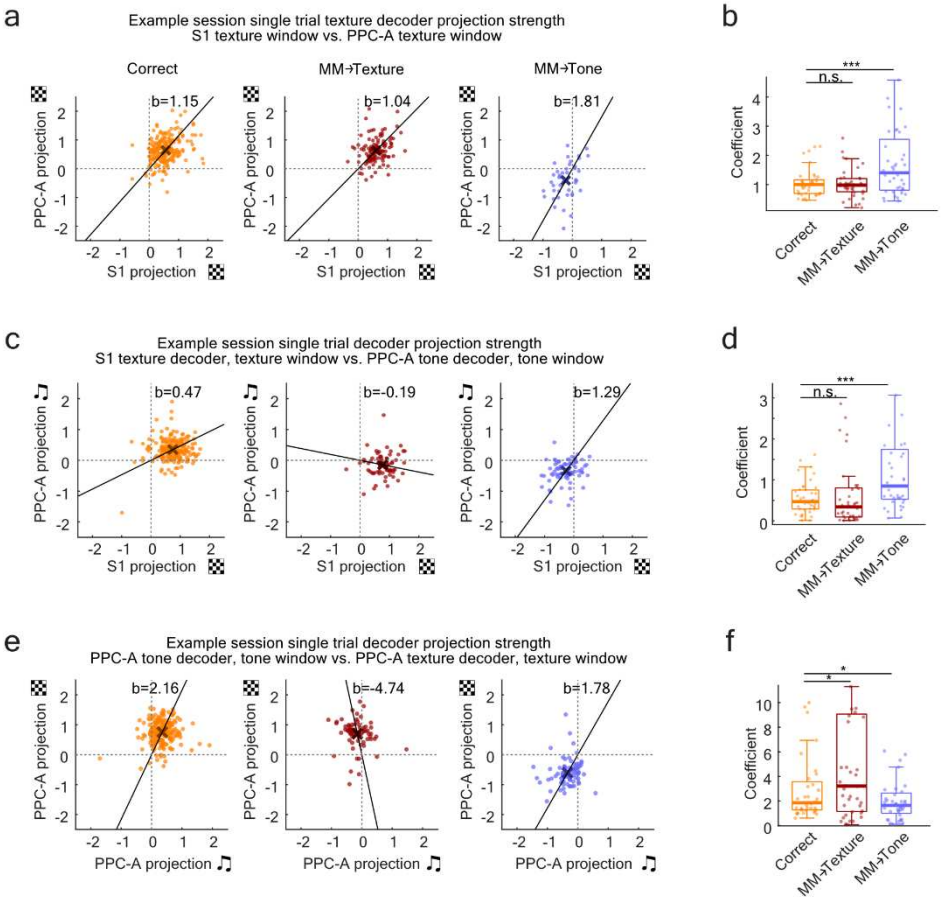

985

Extended Data Figure 9. Trial-to-trial response analysis of S1 and PPC-A. (**a**) Trial-to-trial S1 texture decoding strength (texture decoder projection strength in texture window) vs. PPC-A texture decoding strength, in an example session. The projection strength is averaged within the corresponding task window, and z-scored within each session. Response coefficient is calculated using the center of mass of all data points
990 (y value divided by x value). (**b**) S1 vs PPC-A texture response coefficient of all sessions, using absolute values. (**c**) Trial-to-trial S1 texture decoding strength (texture decoder projection strength in texture window) vs. PPC-A tone decoding strength (tone decoder projection strength in tone window), in an example session. (**d**) S1 texture vs. PPC-A tone response coefficient of all sessions. (**e**) Trial-to-trial PPC-A tone decoding strength vs. texture decoding strength, in an example session. (**f**) PPC-A tone vs. texture response coefficient
995 of all sessions. (Sample numbers are the same as Fig. 4; Wilcoxon signed-rank test; Supplemental Table 1)

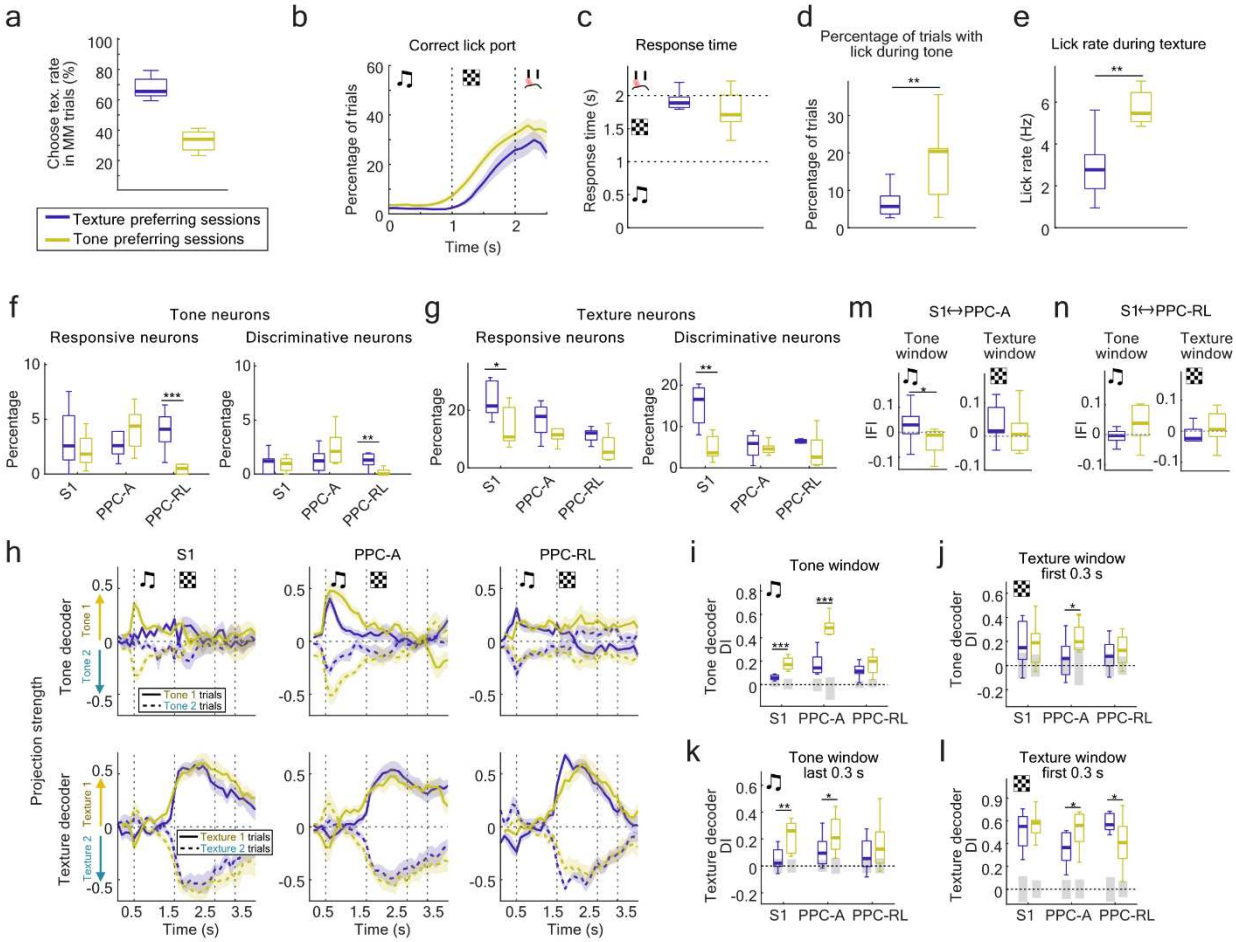

Extended Data Figure 10. Texture-preferring sessions and tone-preferring sessions. (**a**) Rate of choosing texture in mismatch trials, in 10 highest sessions (purple) and 10 lowest sessions (yellow). The 10 highest sessions where mice were prone to choosing texture in mismatch trials were defined as texture-preferring sessions. The 10 lowest sessions were defined as tone-preferring sessions. Color code remains the same for the rest of this figure. (**b**) Lick rate on the correct lick port. (**c**) Response time (p=0.12). (**d**) Percentage of trial with lick during tone. (**e**) Lick rate during texture. (**f**) Percentage of tone responsive neurons (left) and tone discriminative neurons (right) in these sessions. (**g**) Percentage of texture responsive neurons (left) and texture discriminative neurons (right) in these sessions. (**h**) Neuronal population encoding of tone (top panels) and texture (bottom panels) in correct trials. Solid and dash lines indicate texture identity of the trial. (**i**) Tone decoder discrimination index (DI) quantified in tone window. (**j**) Tone decoder DI quantified in the first 0.3 s of texture window. (**k**) Texture decoder AUC quantified in the last 0.3 s of tone window. (**l**) Texture decoder DI quantified in the first 0.3 s of texture window. (**m**) Information flow index of S1-PPC$_A$ interaction in tone window (left) and texture window (right), during correct trials. (**n**) Information flow index of S1-PPC$_{RL}$ interaction in tone window (left) and texture window (right), during correct trials. (3 mice for texture-preferring sessions, 4 mice for tone-preferring sessions; Wilcoxon Rank Sum test; Supplemental Table 1)

Supplementary Table 1. P-values in the manuscript.

Figure	p-value
Fig. 1e	Compared with expert: p=0.0020, 0.0020, 0.0098, 0.0020; compared with tone only: 0.0488
Fig. 1f	p= 0.0273, 0.0488
Fig. 1g	p=4.4830e-19, 4.4830e-19
Fig. 1h	p=0.0084, 1.1619e-11, tested on average of texture window
Fig. 1i	p=0.0283 (one sided)
Fig. 1j	p=0.0002, 0.0104 (one sided)
Fig. 1k	p=0.0001, 0.0015, 0.0089
Fig. 2d	Tone: p=1.4126e-08; texture: p=7.9817e-11; choice: p=4.9107e-06; reward: p= 1.4432e-12, 6.4039e-10
Fig. 2e	Tone: p=7.9418e-10; choice: p=2.7799e-07; reward: p= 3.1870e-11
Fig. 2f	Tone-texture: p=0.0367, 7.3858e-11; texture-choice: p=6.5923e-05; texture-reward: p=1.9059e-07; choice-reward: p=0.0037
Fig. 3c	S1: p= 1.4323e-15, 5.4789e-16, 8.4737e-112; PPC-A: p= 8.8990e-20, 5.1659e-13, 6.6108e-55; PPC-RL: 8.6329e-08, 4.1645e-08, 1.4826e-26
Fig. 4c	Compared with shuffled data: top: S1 p=4.3203e-34, 2.5830e-10, 3.1160e-04, 5.9213e-11, PPC-A p=9.7800e-23, 1.9952e-22, 4.9413e-16, 8.6432e-17, PPC-RL p=6.0660e-21, 3.2090e-08 Between trial types: top: S1 p=2.0369e-05, 3.7612e-04, PPC-A p=1.8325e-04[vs correct], 0.0068[vs mism], PPC-RL p=5.5810e-06, 0.0041
Fig. 4d	Compared with shuffled: S1 p=1.9298e-06, 2.6822e-07, PPC-A p= 3.2050e-04, 0.0139; compared across trial types: S1 p=0.0164, 4.6693e-05[vs correct], 0.0004[vs mism]
Fig. 4e	Compared with shuffled: S1 p=2.3719e-64, 2.0653e-56, 3.4437e-11, PPC-A p=2.1810e-24, 0.0097, 1.5753e-17, 5.3249e-13, PPC-RL p= 6.8567e-39, 5.1950e-07, 1.2797e-36; compared across trial types: S1 p= 2.2052e-18, 8.9334e-08, 2.3936e-16[vs correct], 7.4622e-07[vs incorrect], PPC-A p=3.2124e-07, 2.0661e-04, 3.2124e-07[vs correct], 2.8475e-07[vs incorrect]; PPC-RL p=6.5138e-11, 0.0011, 2.0903e-09[vs correct], 6.2877e-05[vs incorrect])
Fig. 4g	Compared with shuffled: top left: p=3.8432e-05, 0.0334; bottom left: p=3.8432e-05; bottom right: p=5.2468e-07, 2.1029e-05, 0.0058 Comparison between areas: top left: p=0.0108, 0.0477; bottom left: p=0.0063
Fig. 5d	p=2.2938e-04, 0.0023, 0.0023
Fig. 5g	p=0.0100, 0.0204
Fig. 6e	Tone window: p=0.0351, 0.0013; texture window: p=0.0049, 0.0076 (one side)
Fig. 6g	Tone window: p=0.0042 (one side)
Extended Data Fig. 1c	p= 2.7554e-09
Extended Data Fig. 1d	p= 3.9709e-15
Extended Data Fig. 1e	p=0.0065
Extended Data Fig. 1g	0.0147 (one side)
Extended Data Fig. 1h	p=0.0186 (one side)
Extended Data Fig. 1i	p=0.0401, 0.0218

Extended Data Fig. 1m	Tone window: p=1.6248e-10, 3.3100e-04; texture window: p=2.9266e-12, 9.5395e-06; choice window: p=4.9277e-04, 1.6609e-11, 1.4924e-06; reward window: p=6.7886e-12, 0.0100, 2.5266e-04; ITI window: p=1.0898e-05, 4.3163e-04
Extended Data Fig. 2e	Tone neuron: p=1.6899e-04, 0.0327, 0.0078, 0.0402; texture neuron: p= 0.0017, 0.0155; reward neuron: p= 0.0141, 0.0206
Extended Data Fig. 3c	S1: p= 6.9836e-05, 6.5088e-04, 2.5933e-06; PPC-A: p= 0.0043, 0.0239, 2.0700e-46, PPC-RL: p= 6.9366e-07, 0.0013
Extended Data Fig. 4b	S1: p= 3.8504e-15, 4.5298e-13, 1.6075e-80; PPC-A: p= 2.1703e-37, 6.8623e-13, 6.8327e-55; PPC-RL: p= 2.8199e-08, 1.4840e-08, 3.0525e-22
Extended Data Fig. 4d	S1: p=5.7216e-14, 7.9508e-16, 5.4646e-113; PPC-A: p=8.3643e-20, 4.8474e-13, 8.7548e-55; PPC-RL: p=1.3842e-07, 7.7883e-08, 1.0041e-25
Extended Data Fig. 5g	S1: 2.0967e-52, 7.8937e-08, 6.4243e-131, 3.9429e-28, 6.4268e-83; PPC-A: 7.7203e-42, 1.8218e-05, 1.4627e-82, 1.2112e-16, 9.8593e-58; PPC-RL: 5.8268e-17, 2.4701e-05, 1.2193e-65, 5.6878e-24, 2.4171e-43
Extended Data Fig. 6b	Compared with shuffled data: top: S1 p=0.0080, PPC-A p=0.0109, 5.0330e-05, 1.4198e-05, PPC-RL p=0.0044; bottom: S1 p=5.2103e-48, 6.5608e-26, 3.1616e-40, 6.6275e-34, PPC-A p=5.7491e-23, 1.0115e-17, 2.8445e-22, 4.5501e-18, PPC-RL p=1.5158e-30, 1.3736e-06, 7.7303e-32, 9.9296e-14 Comparison between trial types (top: PPC-A p=0.0031, 0.0014; bottom: S1 p=6.5587e-10, 5.7919e-05, PPC-A p=0.0020, PPC-RL p=2.3651e-08, 2.2895e-07
Extended Data Fig. 6c	Top panel, compared to shuffled data: p=5.0438e-26, 9.8588e-17, 1.0282e-12, 1.3982e-04, 1.4672e-09, 3.4750e-05; compared between areas: p=0.0295 Bottom panel, compared to shuffled data: p=2.4486e-59, 1.2376e-24, 5.9757e-34, 1.1554e-05, 0.0063, 2.5388e-06, 9.4988e-46, 1.1077e-06, 2.1090e-27, 9.3130e-08; compared between areas: p=2.4071e-04, 1.4038e-04
Extended Data Fig. 6e	Compared with shuffled data: top left: p=1.0459e-06; top right: p=9.2264e-05, 1.6164e-05, 1.3840e-06; bottom left: p=1.7571e-04 Comparison between areas: top left: p=0.0024; bottom left: p=0.0216
Extended Data Fig. 6f	S1: p=1.1076e-10, 1.1076e-10, 1.1076e-10, 1.1076e-10; PPC-A: p=0.0350, 1.7344e-06, 1.7344e-06, 1.7344e-06, 1.7344e-06; PPC-RL: p=0.0247, 1.2290e-05, 1.2290e-05, 1.2290e-05, 1.2290e-05
Extended Data Fig. 7c	Tone window: p=0.0053, 0.0264; texture window: p=0.0100, 0.0133 (one side)
Extended Data Fig. 7f	Tone window: p=0.0042, 0.0213 (one side)
Extended Data Fig. 8e	p=0.0247, 0.0167 (one side)
Extended Data Fig. 8g	p=0.0316 (one side)
Extended Data Fig. 8i	tone: p=0.0459, 0.0106; texture: p=0.0459
Extended Data Fig. 8k	p=0.0265
Extended Data Fig. 9b	p=1.0253e-04
Extended Data Fig. 9d	p=4.7115e-06
Extended Data Fig. 9f	p=0.0229, 0.0152
Extended Data Fig. 10d	p=0.0091
Extended Data Fig. 10e	p=0.0022
Extended Data Fig. 10f	p=0.0006, 0.0018
Extended Data Fig. 10g	p=0.0173, 0.0046
Extended Data Fig. 10i	p=7.6854e-04, 1.8267e-04

Extended Data Fig. 10j	p=0.0312
Extended Data Fig. 10k	p= 0.0046, 0.0452
Extended Data Fig. 10l	p=0.0452, 0.0452
Extended Data Fig. 10m	p=0.0376

Supplemental Figure 1. CCA results with 0.3 s time window.

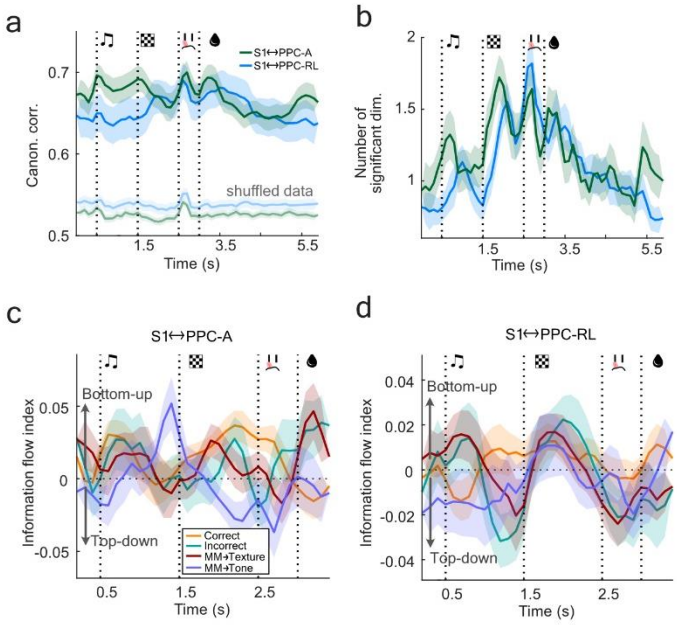

(**a**) Top canonical correlation between S1 and PPC-A (green), and S1 and PPC-RL (blue), using a 0.3-s sliding window. Light colors indicate shuffled correlation, where only the trial correspondence between the two areas were shuffled, while trial structure was kept the same. (**b**) Number of significant dimensions in S1 and PPC-A, and S1 and PPC-RL pairs, using a 0.3-s sliding window. (**c**). Information flow index of S1 and PPC-A interaction, using a 0.3-s sliding window. (**d**) Information flow index of S1 and PPC-RL interaction, using a 0.3-s sliding window. (S1↔PPC-A: 9 mice, 40 sessions; S1↔PPC-RL: 13 mice, 71 sessions)